The H$_2$O southern Galactic Plane Survey (HOPS): I. Techniques and H$_2$O maser data

A. J. Walsh[1][*], S. L. Breen [2], T. Britton[2], K. J. Brooks[2], M. G. Burton[3],
M. R. Cunningham[3], J. A. Green[2], L. Harvey-Smith[2], L. Hindson[2,4], M. G. Hoare[5],
B. Indermuehle[2], P. A. Jones[2,6], N. Lo[6,7], S. N. Longmore[8], V. Lowe[2,3], C. J. Phillips[2],
C. R. Purcell[5], M. A. Thompson [4], J. S. Urquhart[2], M. A. Voronkov[2]
G. L. White[1] and M. T. Whiting[2]

[1]*School of Engineering and Physical Sciences, James Cook University, Townsville, QLD 4811, Australia;*
[2]*CSIRO Astronomy and Space Science, PO BOX 76, Epping, NSW 1710, Australia;*
[3]*School of Physics, University of New South Wales, Sydney, NSW 2052, Australia;*
[4]*Centre for Astrophysics Research, Science and Technology Research Institute, University of Hertfordshire, AL10 9AB, UK;*
[5]*School of Physics and Astronomy, University of Leeds, Leeds, LS2 9JT, UK;*
[6]*Departamento de Astronomía, Universidad de Chile, Casilla 36-D, Santiago, Chile*
[7]*Laboratoire AIM Paris-Saclay, CEA/Irfu - Uni. Paris Didérot - CNRS/INSU, 91191 Gif-sur-Yvette, France*
[8]*Harvard-Smithsonian Center for Astrophysics, 60 Garden Street, Cambridge, MA 02138, USA*

25 May 2011

ABSTRACT

We present first results of the **H$_2$O** **S**outhern Galactic **P**lane **S**urvey (HOPS), using the Mopra radiotelescope with a broad band backend and a beam size of about $2'$. We have observed 100 square degrees of the southern Galactic plane at 12 mm (19.5 to 27.5 GHz), including spectral line emission from H$_2$O masers, multiple metastable transitions of ammonia, cyanoacetylene, methanol and radio recombination lines. In this paper, we report on the characteristics of the survey and H$_2$O maser emission. We find 540 H$_2$O masers, of which 334 are new detections. The strongest maser is 3933 Jy and the weakest is 0.7 Jy, with 62 masers over 100 Jy. In 14 maser sites, the spread in velocity of the H$_2$O maser emission exceeds $100 \, \mathrm{km \, s^{-1}}$. In one region, the H$_2$O maser velocities are separated by $351.3 \, \mathrm{km \, s^{-1}}$. The rms noise levels are typically between 1-2 Jy, with 95% of the survey under 2 Jy. We estimate completeness limits of 98% at around 8.4 Jy and 50% at around 5.5 Jy. We estimate that there are between 800 and 1500 H$_2$O masers in the Galaxy that are detectable in a survey with similar completeness limits to HOPS. We report possible masers in NH$_3$ (11,9) and (8,6) emission towards G19.61-0.23 and in the NH$_3$ (3,3) line towards G23.33-0.30.

Key words: surveys – masers – stars: formation – ISM: molecules – radio lines: ISM – Galaxy: structure

1 INTRODUCTION

Understanding how the interstellar medium (ISM) is linked to stellar birth and death in our Galaxy is a major problem in astrophysics today. In order to understand the processes involved, it is often useful to conduct large-scale Galactic plane surveys. Such surveys as the International Galactic Plane Survey (Taylor et al. 2003; McClure-Griffiths et al. 2005; Stil et al. 2006) in HI, as well as surveys of ^{12}CO (Dame, Hartmann & Thaddeus 2001)

and ^{13}CO (Jackson et al. 2006) have been widely used in tracing out Galactic structure and motions. But these popular tracers are typically insensitive to high density gas. In order to understand the processes at the beginning of star formation, where gas and dust have accumulated to high density regions, it is necessary to choose a tracer of such high densities, as well as other signposts of star formation activity.

We have completed a survey of 100 square degrees of the southern Galaxy in multiple spectral lines, using the Mopra radiotelescope in the 12 mm band (HOPS - The **H$_2$O** southern Galactic **P**lane **S**urvey). Our main target lines are

[*] E-mail: andrew.walsh@jcu.edu.au

the H_2O ($6_{1,6}$–$5_{2,3}$) maser line, NH_3 (1,1), (2,2) and (3,3) inversion transitions, radio recombination lines H62α and H69α and HCCCN (3–2).

H_2O masers are an important signpost of unusual astrophysical conditions such as outflows and shocked gas. They are known to occur in both high and low-mass star forming regions (eg. Forster and Caswell 1999; Claussen et al. 1996), late M-type stars (Dickinson 1976), planetary nebulae (Miranda et al. 2001), Mira variables (Hinkle & Barnes 1979), Asymptotic Giant Branch stars (Barlow et al. 1996) and the centres of active galaxies (Claussen et al. 1984). The majority of currently known H_2O masers are found towards regions of star formation within our Galaxy. However, an untargeted survey is required to determine the relative occurrence of bright H_2O masers with other types of astrophysical objects. There is some evidence that within star forming regions, H_2O masers may be observable at very early stages (eg. Forster and Caswell 2000) of evolution. There is evidence that methanol masers may also be visible at these early stages (eg. Walsh et al. 1998). The relative occurrence of these two masers can be assessed through the two untargeted surveys: the Methanol Multibeam Survey (Green et al. 2009) and HOPS, described here. Recent research has focused on determining parallax distances to H_2O masers (eg. Imai et al. 2007). A long term goal is to accurately establish the dimensions of our Galaxy using bright maser sources throughout the Galaxy (eg. Reid et al. 2009). It is hoped that the bright H_2O masers discovered in HOPS may be used for such distance determinations.

Thermal NH_3 emission in our Galaxy typically traces high density ($\sim 10^4 cm^{-3}$; Evans 1999) gas. Properties of NH_3 spectral line emission can be used to understand the physical conditions of the gas. Lower order (J,K) inversion transitions of NH_3 commonly display hyperfine structure (eg. Ho & Townes 1983) which can be used to calculate the optical depth of the emission, to reduce confusing factors of optically thick emission, when trying to measure the total column density of gas. Multiple inversion transitions of NH_3 are also commonly seen, which can be used to estimate the temperature of the excited gas. These inversion transitions occur within a few GHz of each other, making it possible to observe them simultaneously with the same telescope and similar setup. This greatly eliminates sources of uncertainty when comparing multiple transitions, which in turn makes interpretation more reliable.

In cold, dense regions most molecules and ions are known to freeze-out onto dust grains, with CO, CS and HCO^+ being classic examples (Bergin & Langer 1997; Willacy, Langer & Velusamy 1998; Caselli et al. 1999; Tafalla et al. 2002; Bergin et al. 2002). Thus, such species are unreliable tracers of the densest and coldest regions in our Galaxy. CO also has a low effective critical density $\sim 10^2 cm^{-3}$ (Evans 1999) making it a better tracer of diffuse gas and susceptible to becoming optically thick in dense regions. CO, CS and HCO^+ are also known to be good tracers of outflow activity in star forming regions. Therefore a Galactic map of emission in these tracers can be difficult to interpret in terms of identifying quiescent gas. On the other hand, NH_3 appears to be more robust than CO, CS or HCO^+ against freeze-out onto dust grains (eg. Aikawa et al. 2001). This means that NH_3 can be used to probe the colder denser regions. In addition to this, N_2H^+, which is found under

conditions very similar to NH_3, is known to avoid regions of outflow (eg. Walsh et al. 2007a), tracing only the quiescent gas on large scales. This makes NH_3 a very reliable tracer of cool, dense gas. Combined with the information derived from NH_3 hyperfine structure and multiple inversion transitions, NH_3 can be used to reliably characterise the dense, quiescent gas component of the ISM.

In this paper, we concentrate on describing the survey as well as presenting global properties of the H_2O maser data. In Paper II (Purcell et al. 2011, *in preparation*) we will present the NH_3 (1,1) and (2,2) data and cloud catalogue as well as describing the emission finding algorithm. Paper III (Longmore at al. 2011, *in preparation*) will detail the thermal line fitting routines used on the NH_3 data and will present the physical properties of the unresolved clouds in the catalogue. Results from other spectral lines will be reported in later papers. In follow-up work, we will accurately measure the positions of the H_2O masers using the Australia Telescope Compact Array (ATCA).

2   MOPRA CHARACTERISATION

The Australia Telescope National Facility Mopra telescope is a 22 m antenna located 26 km outside the town of Coonabarrabran in New South Wales, Australia. It is at an elevation of 850 metres above sea level and at a latitude of 31° south.

The receivers use Indium Phosphide High Electron Mobility Transistor (HEMT) Monolithic Microwave Integrated Circuits (MMICs) as the amplifying elements. The receiver systems require no tuning and include noise diodes for system temperature determination. The nominal operating range for the 12 mm receiver is from 16 to 27 GHz, however we have found the receiver still performs well at frequencies as high as 27.5 GHz. Further general information on Mopra can be found in Urquhart et al. (2010).

2.1   The Mopra Spectrometer

The Mopra Spectrometer (MOPS) is the digital filterband backend used for the observations. It comprises an 8.3 GHz total bandwidth, split into four overlapping intermediate frequencies (IFs), each with a width of 2.2 GHz. MOPS can be configured in two modes, either broadband mode, where the full 8.3 GHz is available, or in zoom mode, which was used for HOPS. In zoom mode, each of the four IFs contains four zoom bands of 137.5 MHz each, available to take spectra. The positioning of the four 137.5 MHz zoom bands within each IF is highly flexible, which allows the user to observe virtually any of up to four spectral windows within each 2.2 GHz IF. Thus, it is possible to simultaneously observe up to 16 spectral windows throughout the full 8.3 GHz bandwidth. Each spectral window consists of 4096 channels, which is equivalent to a bandwidth and velocity resolution of 2114 km s^{-1} and 0.52 km s^{-1} at 19.5 GHz, or 1499 km s^{-1} and 0.37 km s^{-1} at 27.5 GHz, respectively. Table 1 gives the details of centre frequencies for each band we observed, as well as the stronger spectral lines found within the bands.

For the H_2O maser observations, two contiguous bands (5 and 6) can be used together to search for masers in the

Table 1. MOPS zoom band settings and strong lines found in each band. The first column lists the MOPS band number, with the total frequency range covered given in the second column. The third column lists the spectral lines that we might detect in HOPS. The spectral line frequency is given in column 5. Column 6 indicates whether the spectral line is a thermal line, a maser line or both. The last column give the reference for the spectral line frequency. Spectral lines that were detected in HOPS are shown in bold.

Band	Frequency Range covered (MHz)	Spectral Line	Frequency (MHz)	Maser or Thermal[1]	Frequency Reference
1	19518 - 19655	**H69α**	19591.110	thermal	Lilley & Palmer (1968)
2	19932 - 20069	CH$_3$OH $(2_{1,1}-3_{0,3})$E	19967.396	maser (II)	Mehrotra et al. (1985)
3	20691 - 20828	**NH$_3$(8,6)**	20719.221	both	Poynter & Kakar (1975)
3	20691 - 20828	NH$_3$(9,7)	20735.452	thermal	Poynter & Kakar (1975)
3	20691 - 20828	NH$_3$(7,5)	20804.830	thermal	Poynter & Kakar (1975)
4	21036 - 21173	**NH$_3$(11,9)**	21070.739	both	Poynter & Kakar (1975)
4	21036 - 21173	NH$_3$(4,1)	21134.311	thermal	Poynter & Kakar (1975)
5	22145 - 22277	**H$_2$O $(6_{1,6}-5_{2,3})$**	22235.080	maser	Kukolich (1969)
6	22278 - 22415	C$_2$S (2_1-1_0)	22344.030	thermal	Kaifu et al. (1987)
7	23037 - 23174	CH$_3$OH $(9_{2,7}-10_{1,10})$A$^+$	23121.024	maser (II)	Mehrotra et al. (1985)
7	23037 - 23174	NH$_3$(2,1)	23098.819	thermal	Kukolich & Wofsky (1970)
8	23382 - 23519	**H65α**	23404.280	thermal	Lilley & Palmer (1968)
8	23382 - 23519	**CH$_3$OH $(10_{1,9}-9_{2,8})$A$^-$**	23444.778	maser (I)	Mehrotra et al. (1985)
9	23658 - 23795	**NH$_3$(1,1)**	23694.471	thermal	Kukolich (1967)
9	23658 - 23795	**NH$_3$(2,2)**	23722.634	thermal	Kukolich (1967)
10	23796 - 23933	**NH$_3$(3,3)**	23870.130	both	Kukolich (1967)
11	24900 - 25037	**CH$_3$OH $(3_{2,1}-3_{1,2})$E**	24928.707	maser (I)	Müller et al. (2004)
11	24900 - 25037	**CH$_3$OH $(4_{2,2}-4_{1,3})$E**	24933.468	maser (I)	Gaines et al. (1974)
11	24900 - 25037	**CH$_3$OH $(2_{2,0}-2_{1,1})$E**	24934.382	maser (I)	Gaines et al. (1974)
11	24900 - 25037	**CH$_3$OH $(5_{2,3}-5_{1,4})$E**	24959.079	maser (I)	Mehrotra et al. (1985)
11	24900 - 25037	**CH$_3$OH $(6_{2,4}-6_{1,5})$E**	25018.123	maser (I)	Mehrotra et al. (1985)
12	25038 - 25175	**CH$_3$OH $(7_{2,5}-7_{1,6})$E**	25124.872	maser (I)	Mehrotra et al. (1985)
12	25038 - 25175	NH$_3$(6,6)	25056.025	both	Kukolich & Wofsky (1970)
13	26556 - 26693	**HC$_5$N (10–9)**	26626.533	thermal	Jennings & Fox (1982)
14	26832 - 26969	**H62α**	26939.170	thermal	Lilley & Palmer (1968)
14	26832 - 26969	CH$_3$OH $(12_{2,10}-12_{1,11})$E	26847.205	maser (I)	Müller et al. (2004)
15	27246 - 27383	**HCCCN (3–2)**	27294.078	thermal	Lafferty & Lovas (1978)
16	27384 - 27521	**NH$_3$(9,9)**	27477.943	thermal	Poynter & Kakar (1975)
16	27384 - 27521	CH$_3$OH $(13_{2,11}-13_{1,12})$E	27472.501	maser (I)	Müller et al. (2004)

[1]CH$_3$OH masers are identified as either Class I or II.

velocity range of -2424 to $+1216\,\mathrm{km\,s^{-1}}$. At the H_2O maser frequency, each channel corresponds to $0.45\,\mathrm{km\,s^{-1}}$.

2.2 Mopra beam shape

Bright water masers can be used to assess the shape of the Mopra beam at 22 GHz. However, due to their highly variable nature, water masers are not used to determine the efficiency of the telescope. The bright water maser G331.51-0.09 was mapped as part of HOPS. The strongest emission is found in the spectral channel at velocity $-89.02\,\mathrm{km\,s^{-1}}$ and is shown in Figure 1. This Figure shows two diffraction rings around the maser peak. We note that a secondary water maser site (G331.44-0.19) coincides with the outer ring from G331.51-0.09 and can be seen in Figure 1. There is also a maser (G331.56-0.12) that is located close to the inner ring, but the maser emission is not significant at this radial velocity and is thus not seen in the Figure. Due to the confusion with G331.44-0.19, we do not fit the rings around G331.51-0.09. Instead, the maser G330.96-0.18, shown in Figure 1 is used, which also shows the inner beam ring and does not appear to have any other confusing masers nearby.

In Figure 2, we show an azimuthally averaged histogram for G330.96-0.09. The histogram shows both the inner and outer beam rings. The inner ring occurs at a radius of about $3.8'$ and contains approximately 14% of the flux of the main peak. The outer ring occurs at about $8.3'$ and contains approximately 3.5% of the flux of the main peak. We estimate the FWHM of the beam from the radial profile to be $2.2'$.

Recent observations by Urquhart et al. (2010) of the water masers in Orion-KL have been used to characterise the Mopra radiotelescope. We find that the positions and intensities of the rings, as well as the size of the beam that we derive above agree well with their results.

2.3 Mopra efficiency and stability

We adopt values from Urquhart et al. (2010) for the main beam size ($2.2'$ at 22.2 GHz), efficiency (0.54 at 22.2 GHz) and Jy K^{-1} conversion factor (12.5 at 22.2 GHz).

During the course of the HOPS observations, we regularly performed observations of a number of well known line sources in the sky, including Orion. These observations were typically conducted once each night and consisted of a position-switch with 2 minutes on-source integration. The standard HOPS zoom configuration was used (Table 1). The purpose of these observations is to assess the stability of the telescope system over time and through different observing
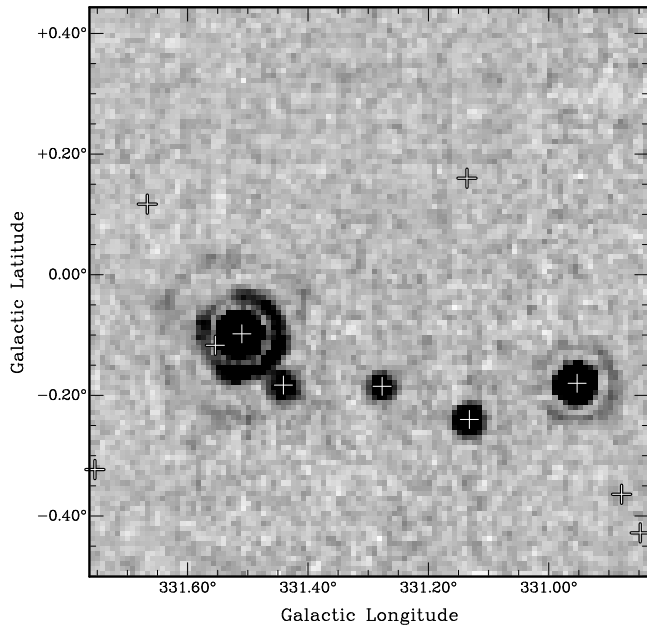
Figure 1. Water maser emission in one spectral channel at $-89.02\,\mathrm{km\,s^{-1}}$. Two strong masers can be seen - G331.51-0.09 (left) and G330.96-0.18 (right) - which both show diffraction rings. Plus symbols indicate the positions of identified water masers. Since the image is only a single channel of the data cube, not all masers are seen in the image, as they do not all emit at this velocity.
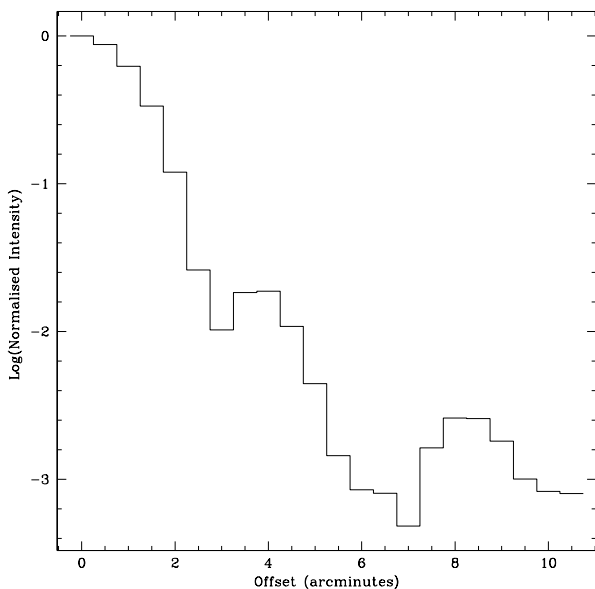

Figure 2. Azimuthally averaged beam profile around the water maser G330.96-0.18. The intensity scale has been normalised to the brightest pixel at the centre and is shown with a log scale on the y-axis.

conditions. Whilst the zoom configuration includes strong maser lines, especially the H_2O maser line, we did not use this line for our calibration as the intensity is known to vary with time (Felli et al. 2007). Instead, we found the strong radio recombination emission lines (H69α and H62α) well suited for calibration, as they are not expected to significantly vary in intensity over the timescale of our observations.

We measure the integrated intensity of the lines by fitting the spectrum with a single gaussian curve and determining the area under that curve, using standard routines in the ASAP software package[1].

Figure 3 shows the distribution of measured integrated intensities for both radio recombination lines throughout the observations. Filled circles indicate integrated intensities for the H69α line and open squares indicate integrated intensities for the H62α line. We might expect that if there is significant atmospheric attenuation, then the integrated intesities might be correlated with elevation and/or system temperature. However, Figure 3 shows that the distribution of integrated intensities for each line does not appear to correlate with either elevation or system temperature. But Figure 3 does show a scatter of integrated intensities. We calculate the standard deviation of integrated intensities is 15 per cent for H69α and 16 per cent for H62α. Thus, about 95 per cent (two standard deviations) of all integrated intensities are within 30 per cent of the mean integrated intesity. We assign 30 per cent as the uncertainty in the intensities of the HOPS data. Since the radio recombination line emission in Orion is extended, it is possible that the actual uncertainty is less then this as some of the scatter in Figure 3 may be due to small pointing errors of the telescope. Thus we consider 30 per cent as an upper limit.

Figure 3 does show a significant difference in the integrated intensities of the two radio recombination lines, with the H62α line weaker than the H69α line, on average. Figure 4 shows the distribution of the ratio of H69α/H62α integrated intensities for simultaneous observations. The mean of this distribution is 1.37, with a standard deviation of 0.07. This shows that the ratio of intensities appears stable over time. Therefore, whilst the absolute intensity scale may be uncertain by a factor of 30 per cent, the relative intensity scale of different spectral lines measured using simultaneous observations is likely to be no worse than 5 per cent. We note that the higher intensity of the H69α line, compared to the H62α line is most likely because the beam at 19.6 GHz (the H69α line frequency) is larger than at 26.9 GHz (the H62α line frequency) and encompasses more extended radio recombination line emission.

3   SURVEY DESIGN

Previous observations of the Galactic plane in continuum (Schuller et al. 2009), thermal line (Jackson et al. 2006; Dame, Hartmann & Thaddeus 2001) and methanol maser emission (Walsh et al. 1998; Green et al. 2009) indicate that molecular material is concentrated in a region within about
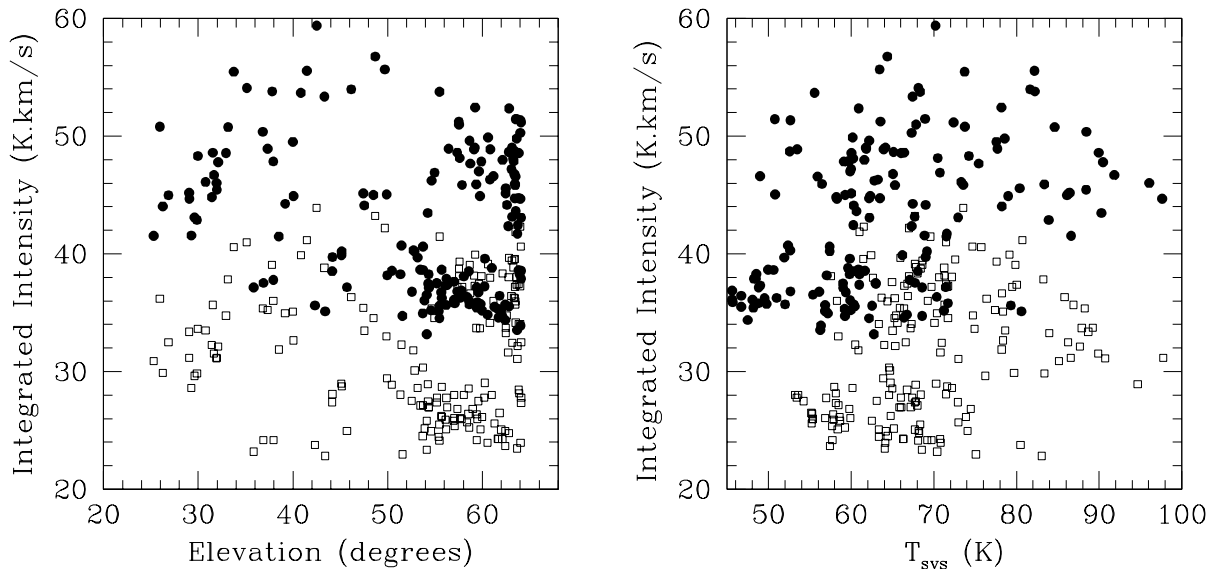
Figure 3. Distribution of integrated intensities for the H69α line (filled circles) and H62α line (open squares) in Orion, plotted against Elevation (left) and system temperature (right). The distributions show there is a spread of integrated intensities, implying that there is an inherent uncertainty in the HOPS absolute flux scale of about 30 per cent.
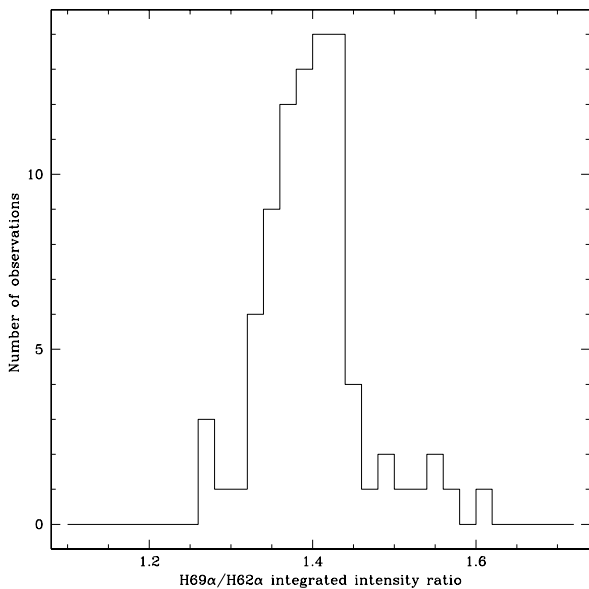

Figure 4. Distribution of the ratio of H69α/H62α integrated intensities in Orion. The ratio has a mean of 1.37 and standard deviation of 0.07, showing that the ratio of intensities is well defined.

30° in Galactic longitude of the Galactic centre. The survey region for HOPS was tailored to cover the bulk of this emission, where the nominal survey region covered Galactic longitudes $290° < l < 360°$ and $0° < l < 30°$. The bulk of methanol masers (Walsh et al. 1998; Green et al. 2009) appear to be confined to within half a degree of the Galactic Plane and H_2O and methanol masers are commonly found in the same star forming regions, so the survey covered nominal Galactic latitudes from $-0.5° < b < +0.5°$. Our choice

of survey region was also based on the amount of observing time that would be reasonably allocated in order to complete the project.

Based on our pilot observations (Walsh et al. 2008), we found the most suitable method was to divide the survey region into blocks of 0.5° by 0.5°. Each block was observed twice in the on-the-fly (OTF) mapping mode, scanning once in Galactic longitude and once in Galactic latitude. Adjacent scans were separated by 51″, to give Nyquist sampling of the beam at the highest observing frequency (27.5 GHz). At lower frequencies, the observations consequently oversample the mapped region. The scanning rate was $15'' \, \mathrm{s}^{-1}$ and spectra were stored every 2 seconds, giving a 30″ spacing between spectra in each row. Each block requires about 2 hours of continuous observations to complete. Thus, each square degree of sky requires approximately 8 hours to be fully observed. We calculate that each position was observed for effectively one minute on-source, using this method.

The positions of reference observations for the 0.5° by 0.5° blocks were chosen to typically lie at b=+0.6° or b=-0.6°, close to one corner of each block. Each reference position was initially checked for emission with a position switch observation, with 2 minutes on-source integration time. Any potential reference position showing emission was discarded and a new reference position was chosen and checked in the same manner.

In order to minimise variations in sensitivity across the survey region, observations were generally limited to elevations greater than 30°, although observations were occasionally made at slightly lower elevations during exceptionally good weather conditions. During good weather and at high elevation, typical system temperatures were 50 K at 19.5 GHz and 65 K at 27.5 GHz. We discarded all data with a system temperature of over 120 K. This upper limit was usually reached when observing through average weather conditions close to an elevation of 30° or during poor weather conditions. We also discarded data where the system tempera-

ture varied quickly due to clouds passing through the telescope beam. Such variations were typically 20 K or greater and had the effect of producing striped features in the reduced data.

Pointing observations were conducted at the start of the survey at a variety of positions across the sky. We found that the global pointing model of Mopra was never more than 15 arcseconds from the true position. We estimate that for the majority of HOPS observations the pointing was better than 10 arcseconds, which is less than 10% of the beam width. Consequently, regular pointing updates were not used, in favour of the global pointing model.

4   DATA REDUCTION

Data were initially reduced using LIVEDATA and GRIDZILLA[2], which are both AIPS++ packages written for the Parkes radiotelescope and adapted for Mopra. LIVEDATA performs a bandpass calibration for each row along the scanning direction, using the preceding reference scan. A first order polynomial (ie. a straight line) is fit to the baseline and then subtracted. In order to minimise the effects of noisy channels at the start and end of each zoom window, the first and last 150 channels were masked before performing the baseline fitting.

GRIDZILLA regrids and combines the data from multiple scanning directions onto a data cube. We chose to regrid onto pixels of 30×30 arcseconds. Data were automatically weighted according to their system temperature and data with system temperatures above 120 K were discarded. Data cubes were then processed in MIRIAD to smooth and/or bin the data, before the creation of peak temperature maps, which were used to find sources of emission. Peak temperature maps are created in MIRIAD, using the "moment=-2" option in the task MOMENT. Peak temperature maps are two-dimensional maps similar to moment zero, (integrated intensity) maps more commonly used in radio astronomy, but each pixel in the two-dimensional peak temperature map corresponds to the highest intensity pixel of the spectrum from the full data cube, at each position on the sky. We found that the peak temperature maps were more sensitive than moment zero maps in detecting weak emission, especially with imperfect baselines and wide bandwidths that were features of the HOPS data.

5   SOURCE FINDING

We employed a variety of methods to detect H_2O maser emission. These same methods were used to detect other rarer masers (see §7.3). Initially, we smoothed the data with a 90×90 arcsecond two-dimensional Gaussian kernel. We found that this size effectively reduced the noise by about 15%, compared to the maser emission. This kernel is slightly smaller than the size of the beam ($132''$), however, we found that a smoothing kernel the size of the beam produced maps that were not as sensitive to identifying weak masers close to the noise level.

After smoothing, the data were converted to peak temperature maps. These maps were visually inspected for maser candidates. Masers were initially identified by inspecting the spectrum at the position of a maser candidate in the peak temperature map and looking for a peak that contained at least two adjacent channels where at least one channel was greater than $3 \times$ the rms noise level and where the sum of all emission channels was greater than $5 \times$ the rms noise level. These values were chosen as they appear to give the best efficiency for detection of real features, with little contamination. Any weak maser candidates were then followed up with a position-switch observation, with 2 minutes on-source integration time, which typically had rms noise levels a factor of 1.4 better than the original map. Any maser candidate that was not seen in the followup spectrum was considered spurious and discarded.

After identifying masers with the above method, the spatially-smoothed data cube was then spectrally binned (along the velocity axis), with three channels combined into each bin. A new peak temperature map was made from this spatially-smoothed and spectrally-binned map then visually inspected for other masers. This method was used because some masers show line widths significantly greater than the channel width ($0.45 \, \mathrm{km \, s^{-1}}$). Binning the data in this way allows us to pick out weak masers with line widths approximately $1.4 \, \mathrm{km \, s^{-1}}$. We also binned the data with eight channels per bin, but did not find any new detections over the unbinned and 3-channel binned data.

We note that our method is well suited to finding weak H_2O masers that typically have large enough line widths to appear in more than one channel. However, the method may miss some weak methanol masers, which are known to have very narrow line widths, since the methanol maser may appear in a single channel and be flagged as a noise spike.

5.1   Positional Accuracy

The reported positions of H_2O masers (see §6) are based on the position of the brightest emission pixel in the data cube. Whilst the Mopra beam is $2.2'$ at 22.2 GHz, the positions of bright masers should be more accurate than this. Some of the detected H_2O masers have been previously observed with the ATCA (Breen et al. 2010) to higher positional accuracy than our Mopra observations. We can therefore compare the positions of those masers that appear in both surveys. Figure 5 shows the distribution of offsets for the masers we have detected with Mopra, compared to the positions given by Breen et al. (2010). We find that nearly all of our H_2O maser positions are no more than one arcminute offset from the corresponding ATCA position. We also find that the median offset is $20''$, indicating that most of the reported positions of masers are probably no more than $20''$ off the real positions.

We also note that of the 34 maser sites that overlap with (Breen et al. 2010), 9 (ie. 26 per cent) are identified as multiple sites by (Breen et al. 2010) but are not resolved by the Mopra beam in our observations. We expect that many more maser spectra identified in this work may consist of multiple maser sites.
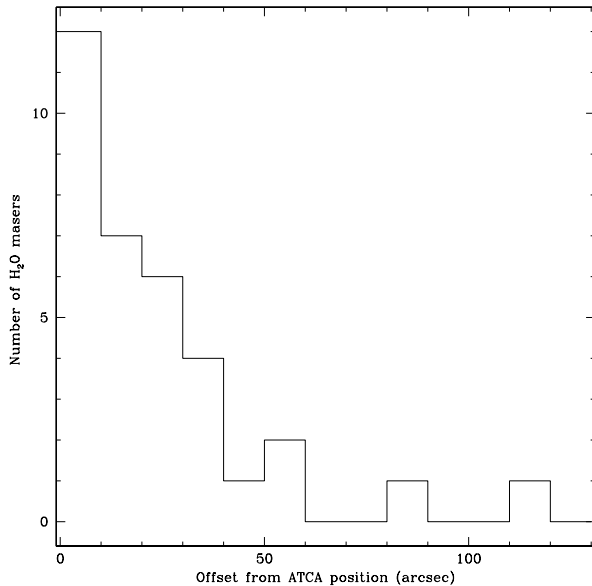
Figure 5. Distribution of Mopra H_2O maser offsets, compared to ATCA positions, using Breen et al. (2010). Note that there are two sites offset by more than $60''$. These are G000.53+0.18 and G337.64+0.15. The emission features in our spectra of these sites lie close to, but not coincident with, emission features from Breen et al. (2010). Thus it is possible that both sites detected in HOPS may be separate to those found by Breen et al. (2010).

6 RESULTS

Here we report results on the H_2O maser emission detected in HOPS. Occasional detections of rare masers are reported in §7.3 and results from other thermal spectral lines such as NH_3, radio recombination lines and HCCCN (3–2) will be reported in later papers.

    H_2O maser emission was found toward 540 distinct sites in the region observed in HOPS. The properties of these sites are summarised in Table 2. The source name (column 1) is derived from the Galactic coordinates. Columns 2 and 3 list the coordinates of the site. Peak flux density, velocity and FWHM of the strongest maser spot in the spectrum are listed in columns 4, 5 and 6, respectively. The minimum and maximum velocities over which emission has been detected are given in columns 7 and 8, respectively. The last column lists whether a maser is a new detection or previously reported. Reference numbers to previously reported masers in the last column are the first detection of the maser and are given in Table 3. Spectra of the masers are presented in Figure 6. The strongest maser (G27.18−0.08) has a peak flux density of 3933 Jy and the weakest maser (G305.56+0.01) has a peak flux density of 0.7 Jy. Note that the weakest maser was detected because it shows a broad line FWHM $(5.0\,\mathrm{km\,s^{-1}})$. The median peak flux density is 11.4 Jy. We detect 62 masers (9%) with peak flux densities over 100 Jy. 334 of the detected H_2O maser sites are new detections (62%). Note that since the Mopra beam for these observations is $2'$ it is likely that many of the maser spectra are composed of multiple maser sites, so that 540 maser sites is almost certainly a lower limit.

Table 3. References for Table 2.

Comment in Table 2	Reference
1	Caswell, Breen & Ellingsen (2011)
2	Breen et al. (2010)
3	Caswell et al. (1983)
4	Genzel & Downes (1977)
5	Mehringer et al. (1998)
6	Benson et al. (1990)
7	Palla et al. (1991)
8	Kazarovets et al. (2006)
9	Batchelor et al. (1980)
10	Brand et al. (1994)
11	Healy et al. (2004)
12	Caswell et al. (1983b)
13	Kleinmann et al. (1978)
14	Deacon et al. (2007)
15	Genzel & Downes (1979)
16	Churchwell et al. (1990)
17	Engels et al. (1986)
18	Forster and Caswell (1989)
19	Codella et al. (1995)
20	Johnston, Sloanacker & Bologna (1973)
21	Jaffe, Guesten & Downes (1981)
22	Urquhart et al. (2009)
23	Benson & Little-Marenin (1996)
24	Nassau, Blanco & Morgan (1954)
25	Caswell et al. (1976)
26	Matthews et al. (1985)
27	Comoretto et al. (1990)
28	Deguchi et al. (2007)
29	Alksnis et al. (2001)
30	Sevenster et al. (2001)
31	Szymczak, Pillai & Menten (2005)
32	Palagi et al. (1993)
33	Wood & Churchwell (1989a)
34	Messineo et al. (2002)
35	Codella et al. (1994)
36	Braz et al. (1989)
37	Deguchi et al. (1989)
38	Caswell et al. (1989)
39	Braz & Scalise (1982)
40	Walsh et al. (2008)
41	Kaufmann et al. (1976)
42	Caswell et al. (1974)
43	Johnston et al. (1972)
44	Caswell & Breen (2010)
45	Sloan & Price (1998)
46	Scalise, Rodriguez & Mendoza-Torres (1989)
47	Breen et al. (2007)
48	Le Bertre, Heydari-Malayeri & Epchtein (1988)
49	Westerlund & Olander (1978)
50	Deacon et al. (2007)
51	Kaufmann et al. (1977)
52	Le Bertre et al. (2003)
53	Taylor, Morris & Schulman (1993)
54	Forster and Caswell (2000)
55	Sjouwerman et al. (2002)

Table 2. Properties of detected water masers. Column 1 lists the source name, derived from the Galactic coordinates. Right ascension and declination coordinates are given in columns 2 and 3, respectively. Properties of the strongest maser spot are given in columns 4, 5 and 6: column 4 lists the peak flux density, column 5 lists the line centre velocity and column 6 lists the line FWHM of the brightest maser spot. For maser sites with multiple maser spots, the minimum and maximum velocity of the maser spots are given in columns 7 and 8, respectively. Otherwise, for maser sites with only a single maser spot, no velocity range is given. Column 9 lists whether the maser site is a new detection ("NEW") or a previous detection. Previous detections are listed as numbers which refer to Table 3. If a previous detection also identifies the maser site with an evolved star, this is also noted. If a previously known evolved star is associated with a newly discovered H_2O maser, then 'NEW' is written, as well as the reference number for the evolved star association.

Source Name	RA (J2000) (h m s)	Dec (J2000) (° ′ ″)	Strongest Maser Spot Peak Flux Density (Jy)	Velocity (km s^{-1})	FWHM (km s^{-1})	Velocity Range Min	Max (km s^{-1})	Comments[1]
G0.05−0.22	17 46 35.9	-29 00 15	7.4	12.4	0.8	11.7	14.7	1
G0.31−0.18	17 47 01.6	-28 46 00	39.2	10.6	0.8	-6.3	21.4	2
G0.31−0.21	17 47 10.3	-28 46 48	6.6	21.5	0.9	10.3	22.4	2
G0.34+0.09	17 46 04.0	-28 36 04	36.6	7.1	0.6			1
G0.37−0.17	17 47 09.7	-28 42 22	22.4	-9.1	0.9	-9.7	-5.2	1
G0.38+0.03	17 46 23.8	-28 35 50	31.8	40.0	1.6	30.3	41.5	3
G0.53+0.18	17 46 09.8	-28 23 29	6.8	-1.4	0.7			2
G0.60−0.00	17 47 03.2	-28 25 18	7.1	37.2	0.9	18.2	75.7	NEW
G0.67−0.04	17 47 20.7	-28 23 13	508.1	70.7	3.8	23.3	127.0	4
G1.01−0.24	17 48 56.4	-28 12 06	4.0	3.4	0.7			NEW
G1.05−0.07	17 48 21.8	-28 04 46	11.1	-37.1	2.8			NEW
G1.15−0.13	17 48 50.0	-28 01 18	177.5	-21.6	1.5	-25.7	-13.0	5
G1.17−0.04	17 48 31.0	-27 57 27	35.4	-22.3	1.6			NEW
G2.53−0.23	17 52 23.7	-26 53 18	4.2	1.5	0.6			NEW
G2.58−0.44	17 53 19.9	-26 56 44	72.6	-6.0	0.8	-25.5	4.8	6
G2.60−0.36	17 53 04.9	-26 53 18	9.1	-20.5	2.1	-21.9	-10.9	NEW
G2.90−0.43	17 54 01.0	-26 40 12	8.6	82.4	1.0			NEW
G2.93+0.28	17 51 22.3	-26 17 16	4.1	-42.8	0.5			NEW
G3.88+0.27	17 53 33.6	-25 28 18	4.3	10.3	0.9			NEW
G4.00+0.33	17 53 34.9	-25 20 07	3.5	13.6	0.9			NEW
G4.00−0.17	17 55 29.5	-25 35 12	2.8	-55.0	7.5			NEW
G4.83+0.22	17 55 51.2	-24 40 13	3.2	11.1	2.7			7
G4.89−0.13	17 57 19.9	-24 47 41	42.8	6.9	1.4			NEW
G5.37+0.05	17 57 41.2	-24 17 33	10.0	2.5	1.1			NEW
G5.52−0.25	17 59 09.9	-24 19 01	2.6	21.9	1.4			NEW
G5.63−0.29	17 59 34.0	-24 14 38	2.5	17.5	1.2			NEW
G5.66+0.42	17 56 57.0	-23 51 36	18.4	18.3	1.0	13.9	19.7	NEW
G5.71−0.50	18 00 31.9	-24 16 28	4.2	12.3	0.9			NEW, 8 - Mira Variable
G5.88−0.39	18 00 29.8	-24 04 06	207.7	9.4	0.9	2.4	11.8	9
G5.90−0.43	18 00 41.6	-24 04 28	7.4	10.1	2.7	7.5	47.0	2
G5.91−0.39	18 00 33.1	-24 02 48	43.0	-61.5	2.2	-64.7	-52.6	2
G6.09−0.12	17 59 54.9	-23 45 34	6.8	3.0	0.7			10
G6.19−0.36	18 01 02.7	-23 47 11	5.9	-29.3	0.8			NEW
G6.20−0.01	17 59 43.4	-23 36 02	2.8	-35.1	4.9	-38.3	-30.4	NEW
G6.23−0.06	17 59 59.5	-23 36 21	4.8	16.9	0.9			NEW
G6.23+0.32	17 58 34.7	-23 24 54	11.9	18.1	1.2	2.4	87.2	NEW
G6.59−0.19	18 01 16.1	-23 21 22	4.6	-2.0	1.0			NEW
G6.61−0.08	18 00 54.7	-23 16 54	29.1	5.3	1.0	-0.7	7.5	2
G6.79−0.26	18 01 58.9	-23 12 57	7.8	11.7	0.8	5.5	13.2	2
G6.92−0.23	18 02 06.2	-23 05 21	8.8	-10.0	3.3	-14.0	-4.8	11
G7.38−0.09	18 02 34.7	-22 37 24	7.6	42.4	1.0			NEW
G7.46−0.28	18 03 27.3	-22 38 29	3.7	23.7	1.8			NEW
G7.47+0.05	18 02 14.1	-22 28 09	42.4	-16.3	1.6	-87.5	-10.3	NEW
G7.54−0.06	18 02 48.5	-22 27 38	4.4	-1.1	3.2			NEW
G8.00−0.27	18 04 34.3	-22 09 57	12.1	36.1	0.8	25.3	43.9	NEW
G8.08+0.15	18 03 11.2	-21 53 30	7.8	22.1	1.1			NEW
G8.20+0.13	18 03 29.2	-21 47 56	10.7	18.4	1.0	0.4	19.6	NEW
G8.32−0.10	18 04 38.0	-21 48 28	4.1	36.9	2.4			NEW
G8.41−0.30	18 05 33.7	-21 49 49	10.3	47.6	1.2			NEW
G8.63−0.24	18 05 48.4	-21 36 07	8.0	1.3	1.0			NEW

[1] "NEW" indicates a newly detected maser, otherwise a number (refer to Table 3) is given for a previous detection. The majority of masers are presumed to be associated with star formation. Previously known associations with evolved stars are referenced, but we await higher precision positions to associate the majority of masers.

Table 2 – *continued ...*

Source Name	RA (J2000) (h m s)	Dec (J2000) (° ′ ″)	Peak Flux Density (Jy)	Velocity (km s^{-1})	FWHM (km s^{-1})	Min	Max	Comments[1]
			Strongest Maser Spot			Velocity Range (km s^{-1})		
G8.67−0.36	18 06 19.7	-21 37 30	29.8	24.7	0.7	-5.5	44.8	12
G8.70−0.43	18 06 38.5	-21 37 57	4.9	32.8	1.3			NEW
G8.73−0.39	18 06 34.2	-21 35 40	6.0	46.7	0.7	30.4	47.4	NEW
G8.83−0.03	18 05 25.7	-21 19 24	38.9	-9.5	1.7	-13.3	-7.2	7
G8.93−0.02	18 05 35.6	-21 13 44	88.9	7.0	0.9	5.7	49.2	13 - M supergiant
G9.10−0.40	18 07 22.8	-21 16 14	18.3	62.9	1.2	-62.0	289.3	14 - water fountain
G9.62+0.19	18 06 15.0	-20 31 43	60.2	5.6	1.7	-9.8	9.1	15
G9.95+0.46	18 05 57.2	-20 06 38	2.9	-65.8	1.1	-66.5	-61.9	NEW
G9.98−0.03	18 07 51.0	-20 19 15	13.4	45.2	1.7	43.7	59.6	7
G10.34−0.14	18 08 59.0	-20 03 58	19.9	19.2	1.1	5.8	35.7	16
G10.39−0.01	18 08 35.3	-19 57 26	7.2	45.9	1.2			NEW
G10.44−0.01	18 08 42.5	-19 54 24	19.7	70.4	1.8	67.8	83.8	2
G10.48+0.03	18 08 37.4	-19 51 28	108.3	70.7	1.1	40.7	88.1	17
G10.62−0.38	18 10 26.1	-19 55 52	381.5	0.3	3.1	-19.4	8.8	18
G10.64−0.50	18 10 56.1	-19 58 35	59.7	-67.9	3.9	-71.8	-46.1	NEW
G10.89+0.13	18 09 07.4	-19 27 20	13.8	23.9	2.2	9.0	26.0	NEW
G10.96+0.03	18 09 38.9	-19 26 18	25.7	24.3	0.5			19
G11.65−0.06	18 11 22.2	-18 52 28	1.4	3.7	6.1	-3.1	30.8	NEW
G11.73−0.18	18 11 57.2	-18 51 53	5.9	-43.0	0.9			NEW
G11.87+0.00	18 11 35.6	-18 39 21	21.6	21.2	0.9	20.2	38.9	NEW
G11.92−0.14	18 12 13.2	-18 40 49	7.1	33.8	0.8	23.8	49.6	12
G11.96−0.16	18 12 22.0	-18 39 09	6.2	40.3	1.4	38.5	45.2	NEW
G12.22−0.09	18 12 38.5	-18 23 39	3.2	20.8	4.6			4
G12.22+0.38	18 10 53.2	-18 09 56	20.9	37.7	0.9			NEW
G12.22−0.33	18 13 31.4	-18 29 57	21.5	-15.8	1.3			NEW
G12.55−0.18	18 13 39.2	-18 08 45	9.4	59.5	0.8			NEW
G12.68−0.18	18 13 53.5	-18 01 31	163.4	58.6	0.8	53.7	61.9	20
G12.82−0.19	18 14 13.3	-17 54 55	2.8	36.1	1.2	30.5	37.4	4
G12.91−0.02	18 13 45.5	-17 45 06	19.4	13.6	2.3			4
G12.92−0.24	18 14 36.4	-17 51 05	5.5	35.6	1.6	28.9	36.3	4
G12.94−0.04	18 13 55.1	-17 44 02	6.1	20.9	0.7			NEW
G12.94−0.07	18 14 00.7	-17 44 45	57.0	33.5	0.7			NEW
G13.19+0.06	18 14 03.2	-17 27 56	9.1	-4.1	3.5			4
G13.44+0.24	18 13 52.9	-17 09 31	9.0	48.2	0.9	40.7	55.4	NEW
G13.46+0.22	18 14 00.4	-17 09 23	7.1	16.4	1.1			NEW
G13.69−0.05	18 15 26.9	-17 04 39	31.9	44.7	0.9			NEW
G13.82+0.27	18 14 32.0	-16 48 58	2.9	70.9	1.3			NEW
G13.88+0.29	18 14 34.8	-16 44 50	20.0	-41.7	1.4	-45.6	-14.0	4
G14.03−0.31	18 17 04.6	-16 54 01	5.9	129	1.0			NEW
G14.11+0.09	18 15 45.3	-16 38 38	47.9	9.2	0.8			21
G14.17−0.05	18 16 23.6	-16 39 35	126.5	54.3	1.3	35.1	57.9	8
G14.20−0.18	18 16 56.9	-16 41 38	27.5	24.1	1.3			NEW
G14.61+0.03	18 16 59.6	-16 14 10	21.9	29.8	0.9	7.6	32.0	21
G14.68−0.05	18 17 24.2	-16 12 47	13.0	-5.2	0.8	-6.7	-0.9	NEW
G14.78−0.36	18 18 43.9	-16 16 16	4.9	31.6	1.3	30.0	34.0	NEW
G15.09+0.21	18 17 16.5	-15 43 22	21.4	28.0	0.9	20.7	32.1	22
G15.54−0.13	18 19 22.3	-15 29 28	4.3	23.1	0.6			NEW
G15.55+0.37	18 17 36.7	-15 14 38	2.0	70.1	2.9			NEW
G15.97+0.24	18 18 53.2	-14 56 09	49.5	58.3	0.6	-98.1	190.5	NEW
G16.05−0.13	18 20 24.7	-15 02 24	13.7	62.2	0.6			NEW
G16.25+0.19	18 19 37.0	-14 42 38	3.7	-1.3	1.7			NEW
G16.28+0.42	18 18 50.7	-14 34 55	1.0	-84.7	3.8			NEW
G16.46+0.44	18 19 06.7	-14 24 32	18.2	21.2	1.5	18.0	46.7	NEW
G16.58−0.04	18 21 07.1	-14 31 38	63.2	63.9	1.3	56.5	69.5	12
G17.55−0.12	18 23 15.8	-13 42 35	477.2	30.6	1.1	28.7	57.2	13
G17.64+0.17	18 22 24.5	-13 29 42	126.7	26.0	1.0	15.7	27.3	23
G17.97+0.09	18 23 18.5	-13 14 36	8.3	26.6	0.8			NEW
G17.98+0.24	18 22 47.8	-13 09 27	15.0	15.4	0.9			22
G18.16+0.39	18 22 36.8	-12 56 14	10.4	55.6	0.9			NEW
G18.24−0.12	18 24 35.2	-13 05 53	8.4	39.1	1.8			NEW
G18.52+0.15	18 24 09.9	-12 43 25	3.0	22.4	3.0			NEW

Table 2 – *continued ...*

Source Name	RA (J2000) (h m s)	Dec (J2000) (° ′ ″)	Peak Flux Density (Jy)	Velocity (km s^{-1})	FWHM (km s^{-1})	Min (km s^{-1})	Max (km s^{-1})	Comments[1]
			Strongest Maser Spot			Velocity Range		
G18.55+0.04	18 24 38.0	-12 45 21	10.7	32.2	0.5	31.3	35.2	NEW
G18.61−0.08	18 25 10.3	-12 45 30	6.0	41.3	1.2	40.0	52.4	NEW
G18.73−0.22	18 25 55.3	-12 42 49	28.5	36.7	1.3	32.2	46.3	NEW
G18.88−0.47	18 27 07.0	-12 41 55	7.7	65.1	1.5			NEW
G19.00−0.23	18 26 27.8	-12 28 57	21.8	-15.9	7.2			NEW
G19.15−0.47	18 27 36.4	-12 27 23	41.0	30.2	0.7	22.1	37.3	NEW, 24 - M supergiant
G19.27+0.09	18 25 48.3	-12 05 25	3.4	28.6	1.9			NEW
G19.47+0.18	18 25 53.3	-11 52 26	5.0	-6.7	2.3	-12.6	20.7	NEW
G19.49+0.16	18 25 58.7	-11 52 14	4.5	27.0	1.1	22.4	28.3	NEW
G19.61−0.23	18 27 37.9	-11 56 32	127.4	41.9	3.4	23.0	57.9	25
G19.71−0.26	18 27 54.7	-11 51 55	6.4	38.9	1.0	38.1	44.1	NEW
G20.08−0.13	18 28 10.3	-11 28 39	19.7	46.4	0.8	37.5	47.4	12
G20.78−0.06	18 29 12.7	-10 49 47	37.8	59.2	1.8			26
G21.04−0.06	18 29 42.9	-10 35 36	5.4	35.6	1.5			27
G21.80−0.12	18 31 21.3	-09 56 56	83.2	106.2	2.1	-53.1	164.7	28 - Water Fountain
G21.81+0.15	18 30 24.6	-09 49 02	7.3	2.7	4.3	-4.7	10.9	NEW, 29 - Carbon Star
G21.88+0.02	18 31 01.8	-09 48 44	17.3	21.4	3.2	18.9	26.2	15
G21.95+0.01	18 31 11.3	-09 45 25	14.6	109.8	0.8	95.6	111.5	23
G22.00+0.07	18 31 03.0	-09 41 10	10.0	147.2	2.3	145.4	152.1	NEW, 30 - OH/IR star
G22.03+0.22	18 30 34.3	-09 35 39	12.7	53.7	0.7			31
G22.82−0.17	18 33 26.8	-09 04 10	7.9	41.0	1.2			NEW
G22.97−0.37	18 34 27.1	-09 01 54	3.3	74.8	2.0			NEW
G23.00−0.41	18 34 38.7	-09 01 05	167.8	68.9	1.3	62.3	82.6	31
G23.15−0.23	18 34 16.8	-08 48 09	19.8	110.2	0.9	108.8	113.3	NEW
G23.21−0.38	18 34 55.7	-08 49 12	13.8	79.4	1.2	77.1	143.5	31
G23.41−0.21	18 34 42.3	-08 33 58	5.0	102.5	1.5	100.8	135.8	32
G23.46−0.35	18 35 18.2	-08 35 12	4.1	105.6	2.3			NEW
G23.48+0.10	18 33 44.1	-08 21 26	10.5	87.0	2.5	49.2	89.5	NEW
G23.91+0.08	18 34 35.2	-07 59 16	3.7	73.1	4.2	71.3	97.9	19
G23.98+0.15	18 34 26.6	-07 53 38	13.8	31.5	1.6			33
G23.98+0.24	18 34 08.1	-07 50 43	11.3	99.8	1.2	94.5	107.6	NEW
G24.33+0.14	18 35 08.3	-07 35 16	16.3	110.9	1.4			31
G24.43+0.09	18 35 30.2	-07 31 19	3.7	111.9	1.4			NEW
G24.45+0.26	18 34 57.3	-07 25 24	10.7	113.9	0.5			NEW
G24.46+0.20	18 35 10.7	-07 26 35	34.0	120.7	1.9	115.7	122.6	NEW
G24.50−0.03	18 36 05.3	-07 30 50	20.1	111.3	0.8	73.7	153.0	13
G24.79+0.08	18 36 12.9	-07 12 04	226.7	111.2	2.4	89.5	116.4	18
G24.94−0.03	18 36 54.5	-07 07 17	10.5	-4.9	1.3			NEW
G24.94+0.08	18 36 31.3	-07 04 18	280.0	42.9	0.6			31
G24.99−0.17	18 37 29.7	-07 08 25	7.5	96.4	1.1			NEW
G25.06+0.27	18 36 02.3	-06 52 44	9.1	77.6	2.2			NEW, 34 - OH/IR star
G25.11−0.03	18 37 13.1	-06 58 27	7.5	101.2	2.2	93.8	109.1	NEW
G25.29−0.04	18 37 35.3	-06 48 52	4.6	114.7	1.4	105.7	119.3	NEW
G25.38−0.18	18 38 15.9	-06 47 56	111.8	68.6	1.0			35
G25.40+0.03	18 37 31.2	-06 41 03	26.1	-15.9	0.7			22
G25.52−0.11	18 38 14.6	-06 38 43	9.1	98.8	0.7			NEW
G25.73−0.11	18 38 37.7	-06 27 38	13.0	97.4	1.3	96.5	105.9	NEW
G25.82−0.05	18 38 35.2	-06 21 06	20.6	125.7	0.7	82.3	127.4	NEW
G25.83−0.18	18 39 02.9	-06 24 07	295.0	90.6	2.6	82.8	97.3	31
G25.91−0.08	18 38 50.7	-06 16 56	14.1	108.6	0.7	102.9	126.2	NEW
G25.98−0.08	18 39 00.0	-06 13 05	11.6	90.0	1.5			NEW
G26.11−0.09	18 39 16.7	-06 06 38	64.2	23.5	1.4	22.1	27.4	22
G26.13−0.03	18 39 06.1	-06 04 08	11.1	84.9	3.0	72.7	101.3	NEW
G26.40−0.10	18 39 50.7	-05 51 17	5.8	98.6	2.8	78.0	101.9	NEW
G26.51+0.28	18 38 40.7	-05 34 53	52.4	103.3	3.6	101.0	108.3	7
G26.53+0.40	18 38 17.4	-05 30 49	11.3	100.9	0.9			NEW
G26.55−0.29	18 40 47.6	-05 48 56	11.5	111.6	3.5	105.0	117.1	NEW
G26.85+0.16	18 39 44.3	-05 20 34	3.3	97.0	1.2	83.0	111.6	NEW
G27.01−0.03	18 40 42.6	-05 17 02	6.3	-15.2	0.9	-19.1	-14.0	NEW
G27.08+0.20	18 40 01.6	-05 06 43	1.0	27.8	13.3			NEW
G27.18−0.08	18 41 11.6	-05 08 53	3932.7	17.5	0.9	13.2	33.6	36

Table 2 – *continued ...*

Source Name	RA (J2000) (h m s)	Dec (J2000) (° ′ ″)	Strongest Maser Spot Peak Flux Density (Jy)	Velocity (km s^{-1})	FWHM (km s^{-1})	Velocity Range Min (km s^{-1})	Max	Comments[1]
G27.33+0.18	18 40 33.7	-04 54 30	20.0	33.9	0.9	33.1	38.4	NEW, 29 - Carbon Star
G27.37−0.16	18 41 49.6	-05 01 24	25.6	88.2	2.2	86.1	98.9	31
G27.41−0.05	18 41 31.1	-04 56 12	5.0	108.7	2.0	100.9	109.9	NEW
G27.50−0.28	18 42 31.1	-04 57 44	2.9	-15.4	1.3	-39.6	-11.2	NEW
G27.60+0.08	18 41 23.7	-04 42 21	4.1	35.4	0.9	23.4	41.6	NEW
G27.70+0.20	18 41 09.7	-04 33 48	2.4	62.1	5.3			NEW
G27.78+0.06	18 41 49.3	-04 33 14	8.3	98.4	1.2	92.4	109.6	31
G27.87−0.23	18 43 00.8	-04 36 47	21.0	12.3	0.7			19
G27.93+0.24	18 41 25.5	-04 20 39	58.1	62.4	1.3	35.4	65.9	37
G28.01−0.43	18 43 57.2	-04 34 38	18.0	19.3	0.6			NEW
G28.21−0.05	18 42 58.9	-04 13 40	23.7	95.4	1.1			NEW
G28.34+0.14	18 42 32.4	-04 01 18	41.3	17.5	2.0			NEW
G28.40+0.08	18 42 51.4	-03 59 50	201.1	77.7	0.7	76.9	86.1	31
G28.41+0.07	18 42 55.8	-03 59 47	26.6	34.5	0.9	21.4	40.3	31
G28.62+0.06	18 43 21.5	-03 48 31	37.7	-3.9	0.7			NEW
G28.65+0.03	18 43 29.6	-03 47 52	8.7	103.8	0.8			NEW
G28.79+0.24	18 43 00.5	-03 34 33	3.0	108.6	5.1			35
G28.81+0.37	18 42 36.5	-03 29 47	18.6	88.3	0.8	83.5	89.3	31
G28.85+0.50	18 42 12.6	-03 24 37	6.3	86.6	4.2	84.2	91.3	31
G28.86+0.07	18 43 46.2	-03 35 21	194.5	105.8	3.0	102.3	107.8	15
G28.88−0.03	18 44 07.9	-03 36 55	5.7	114.9	1.7	101.8	123.8	19
G28.96+0.40	18 42 46.0	-03 20 53	6.2	18.6	2.2			NEW
G29.25−0.24	18 45 34.8	-03 23 10	5.9	106.0	1.8	98.1	120.9	NEW
G29.28−0.13	18 45 13.6	-03 18 13	6.5	40.8	0.7	39.5	52.4	NEW
G29.33−0.16	18 45 25.3	-03 16 53	39.6	47.6	0.9			NEW
G29.49+0.19	18 44 29.1	-02 58 45	4.9	35.4	2.1	31.5	37.9	NEW
G29.92−0.04	18 46 05.1	-02 42 08	36.3	40.5	2.1	15.5	42.5	32
G29.96−0.01	18 46 02.6	-02 38 59	73.5	99.2	2.1	88.5	110.3	4
G29.98+0.12	18 45 38.7	-02 34 13	7.8	102.8	1.1	101.7	122.7	NEW
G291.37−0.21	11 14 08.3	-60 52 34	79.0	3.0	0.5			NEW
G291.58−0.42	11 15 05.2	-61 09 11	343.4	0.7	0.9	-8.5	19.3	38
G291.79+0.39	11 19 07.9	-60 28 04	7.3	-152.5	0.6			NEW
G292.58−0.29	11 23 17.2	-61 22 18	12.4	-14.0	3.1			NEW
G293.59−0.20	11 31 35.6	-61 36 55	17.2	29.4	0.7			NEW
G295.09−0.46	11 43 12.9	-62 17 09	11.1	25.1	1.3	23.9	27.0	NEW
G297.86−0.27	12 07 00.2	-62 41 59	13.1	-19.7	2.0	-20.9	2.5	NEW
G298.20−0.34	12 09 48.4	-62 49 47	3.6	81.0	1.5			NEW
G298.22−0.33	12 09 57.4	-62 49 28	3.2	36.7	1.2	33.1	38.7	39
G298.23−0.38	12 09 57.9	-62 52 31	13.4	40.4	1.1	29.6	41.3	NEW
G298.63−0.36	12 13 32.2	-62 54 47	30.4	40.0	1.5	39.2	44.3	NEW
G298.72−0.08	12 14 36.2	-62 39 11	34.7	18.1	1.3			NEW
G298.88+0.32	12 16 30.9	-62 16 48	26.7	18.4	2.1	9.5	21.1	NEW
G299.00+0.13	12 17 17.6	-62 29 09	115.2	19.3	0.8	-12.3	29.8	39
G300.32−0.27	12 28 24.3	-63 01 12	54.0	33.7	0.8			NEW
G300.50−0.17	12 30 01.1	-62 56 41	241.4	11.0	1.1	-9.0	12.6	38
G301.13−0.22	12 35 32.9	-63 02 21	834.1	-45.8	0.8	-66.8	-28.4	38
G301.35+0.02	12 37 32.9	-62 48 40	4.9	-26.8	0.8			NEW
G301.76+0.29	12 41 13.2	-62 33 23	15.6	-43.7	1.0	-61.5	-19.4	NEW
G302.48−0.03	12 47 28.7	-62 54 09	25.0	-30.9	0.7	-61.4	6.9	NEW
G303.70−0.41	12 58 18.3	-63 16 14	17.1	-54.6	1.0	-62.0	-40.2	NEW
G303.87+0.47	12 59 33.7	-62 23 31	3.5	-63.8	1.3			NEW
G304.06+0.44	13 01 09.5	-62 24 56	10.7	-51.1	1.5	-52.8	-41.4	NEW
G304.07+0.41	13 01 18.3	-62 26 24	18.4	-50.5	0.9			NEW
G304.37−0.34	13 04 09.3	-63 10 31	16.6	29.0	0.8			NEW
G305.01+0.43	13 09 21.7	-62 22 28	12.1	-54.5	1.0			NEW
G305.14+0.07	13 10 41.9	-62 43 02	4.2	-38.4	0.8			40
G305.19−0.00	13 11 13.7	-62 47 20	25.8	33.4	1.7	-47.5	36.6	38
G305.21+0.21	13 11 11.9	-62 34 36	180.0	-39.1	0.8	-47.8	-29.7	41
G305.27−0.00	13 11 52.3	-62 46 52	2.4	-37.9	1.5	-39.1	-32.5	40
G305.32+0.07	13 12 16.8	-62 42 08	903.4	-45.1	0.7	-45.7	-29.0	40

Table 2 – *continued ...*

Source Name	RA (J2000) (h m s)	Dec (J2000) (° ′ ″)	Strongest Maser Spot Peak Flux Density (Jy)	Velocity ($\mathrm{km\,s^{-1}}$)	FWHM ($\mathrm{km\,s^{-1}}$)	Velocity Range Min ($\mathrm{km\,s^{-1}}$)	Max	Comments[1]
G305.36+0.15	13 12 34.3	-62 37 13	457.6	-35.6	3.0	-46.3	-29.7	42
G305.36+0.21	13 12 33.8	-62 33 33	170.9	-33.6	1.2	-90.5	52.7	43
G305.56+0.01	13 14 24.4	-62 44 48	0.7	-37.7	5.0			40
G305.66−0.10	13 15 24.1	-62 50 52	6.7	-68.9	1.8			44
G305.73+0.08	13 15 49.4	-62 39 19	4.1	-43.9	3.8			40
G305.80−0.24	13 16 40.8	-62 58 24	3023.5	-27.6	0.5	-43.2	-24.3	38
G305.82−0.12	13 16 44.8	-62 50 42	4.0	-27.5	0.6	-55.9	-15.6	44
G305.83−0.08	13 16 51.4	-62 48 31	41.2	-114.5	4.3	-120.1	-83.8	44
G305.89+0.02	13 17 14.4	-62 42 21	41.2	-28.3	1.4	-40.4	-26.5	44
G305.95+0.03	13 17 46.8	-62 41 26	3.7	-41.5	1.0			44,45 - AGB Star
G307.13+0.32	13 27 38.3	-62 15 30	87.2	-42.8	0.8			NEW
G307.27+0.08	13 29 05.3	-62 28 17	3.9	-31.0	1.7			NEW
G307.34+0.18	13 29 36.4	-62 21 52	2.8	-93.8	5.3			NEW
G307.80−0.45	13 34 24.6	-62 55 08	47.4	-13.0	1.0			NEW
G307.95+0.03	13 35 00.0	-62 25 18	3.3	-45.0	5.4			NEW
G308.05−0.38	13 36 27.8	-62 48 24	8.0	-12.3	0.7	-17.5	-5.8	NEW
G308.08−0.42	13 36 43.7	-62 50 01	5.1	-16.3	1.2	-17.7	-8.1	NEW
G308.13−0.30	13 37 01.1	-62 42 21	36.1	0.6	0.7			NEW
G308.16−0.45	13 37 29.9	-62 51 13	4.4	5.2	3.1			NEW
G308.61−0.18	13 40 55.9	-62 30 25	2.9	-12.6	3.5			NEW
G308.70−0.00	13 41 23.3	-62 18 48	2.1	-66.3	1.3			NEW
G308.92+0.12	13 43 03.4	-62 09 08	3.7	-50.5	1.0			39
G309.29−0.47	13 47 11.3	-62 38 49	5.2	-5.8	2.4			NEW
G309.38−0.13	13 47 20.8	-62 18 07	8.5	-50.6	0.8			38
G309.90+0.33	13 50 48.5	-61 43 59	6.9	-54.3	0.8	-55.1	-47.0	NEW
G310.34−0.07	13 55 15.2	-62 00 58	6.0	-3.5	3.4			NEW
G310.52−0.22	13 57 03.4	-62 07 12	4.5	55.3	2.3	47.1	58.8	NEW
G310.58+0.38	13 56 19.0	-61 31 45	5.7	-30.8	0.9	-57.4	-28.1	37
G310.88+0.01	13 59 28.4	-61 48 33	15.4	-70.8	1.8	-82.0	-44.2	NEW
G311.23−0.03	14 02 29.7	-61 45 15	162.2	28.0	1.1	16.1	43.4	44
G311.56+0.23	14 04 30.2	-61 24 29	13.3	9.6	2.0	-1.1	12.6	NEW
G311.64−0.38	14 06 38.9	-61 58 35	215.5	32.2	2.2	14.6	52.9	38
G311.72+0.24	14 05 45.1	-61 21 21	108.1	-72.7	1.0	-80.3	-44.5	NEW
G312.07+0.09	14 08 54.7	-61 23 53	15.0	-32.8	1.7	-38.1	5.6	44
G312.11+0.01	14 09 27.1	-61 27 54	11.4	-41.8	1.6	-46.5	-27.6	44
G312.48−0.33	14 13 15.4	-61 40 46	11.7	-31.6	3.4	-43.3	-27.3	NEW
G313.46+0.07	14 19 55.3	-60 58 43	11.5	1.3	1.0			NEW
G313.47+0.20	14 19 38.8	-60 51 28	14.0	-9.7	0.7	-12.2	1.4	38
G313.57+0.32	14 20 04.5	-60 42 23	12.1	-45.2	0.8	-49.0	-39.8	2
G314.23+0.26	14 25 17.8	-60 32 29	6.4	-61.4	1.2			NEW
G314.33+0.11	14 26 29.6	-60 38 45	9.8	-41.8	1.2			2
G314.41+0.05	14 27 17.8	-60 40 12	152.5	-43.8	0.5			NEW
G314.98+0.03	14 31 38.3	-60 28 36	6.3	-54.1	2.2			NEW
G315.22−0.25	14 34 20.2	-60 38 45	6.4	-64.5	2.0			NEW
G315.23−0.11	14 33 57.3	-60 30 45	5.8	-16.2	5.6			NEW
G315.93+0.05	14 38 42.8	-60 05 15	13.6	-7.1	1.1			NEW
G316.09−0.07	14 40 14.5	-60 07 41	6.7	-53.0	0.9			NEW
G316.35−0.37	14 43 07.8	-60 17 43	6.8	1.5	2.4	-14.6	5.7	36
G316.40−0.32	14 43 19.7	-60 13 44	8.3	-11.5	1.5	-18.1	3.2	38
G316.63−0.09	14 44 16.6	-59 55 35	13.6	-21.1	2.9	-24.5	-5.6	9
G316.76−0.02	14 44 55.6	-59 48 21	39.9	-34.9	1.6	-53.2	-32.8	9
G316.81−0.06	14 45 25.5	-59 49 18	311.0	-47.2	1.6	-52.3	-25.7	41
G317.87+0.14	14 52 14.5	-59 10 49	5.1	-3.3	1.0	-4.2	0.7	NEW
G317.87−0.15	14 53 16.2	-59 26 28	18.0	-52.7	1.2	-54.4	-41.4	NEW
G317.98+0.12	14 53 08.7	-59 09 00	4.3	-59.1	0.9	-60.3	-44.5	NEW
G318.05+0.09	14 53 41.7	-59 08 36	805.3	-52.0	3.0	-61.0	-38.3	46
G318.78−0.13	14 59 30.6	-59 00 28	731.0	-135.7	2.7	-144.9	-39.1	NEW
G318.94−0.18	15 00 50.1	-58 58 21	3.7	-33.8	1.4	-38.5	-32.7	38
G319.34−0.32	15 04 04.7	-58 54 13	7.2	-36.0	1.4	-40.7	-34.9	NEW
G319.39−0.01	15 03 13.6	-58 36 13	11.0	-6.4	0.5	-8.9	-0.8	2

Table 2 – *continued ...*

Source Name	RA (J2000) (h m s)	Dec (J2000) (° ′ ″)	Strongest Maser Spot Peak Flux Density (Jy)	Velocity (km s^{-1})	FWHM (km s^{-1})	Velocity Range Min (km s^{-1})	Max	Comments[1]
G319.83−0.19	15 06 52.2	-58 32 47	16.0	-12.1	2.9	-15.6	-0.5	38
G320.23−0.28	15 09 52.8	-58 25 31	5.7	-61.7	1.3	-67.5	-58.9	38
G320.24−0.08	15 09 09.8	-58 14 55	3.7	-9.9	1.1			NEW
G320.26−0.30	15 10 06.6	-58 25 38	7.0	-116.3	2.5	-127.9	-108.4	38
G320.34−0.20	15 10 16.2	-58 17 57	23.8	-107.7	1.3	-118.3	-102.3	NEW
G320.43+0.10	15 09 40.1	-57 59 52	12.3	-10.4	1.0	-16.6	-3.1	NEW
G320.90−0.29	15 14 15.9	-58 05 25	172.0	-35.9	1.6	-39.9	-33.2	47
G321.04−0.50	15 15 58.6	-58 11 41	12.0	-52.4	1.0	-67.3	-51.3	2
G321.38−0.29	15 17 22.5	-57 50 20	3.2	-53.9	0.7	-60.0	47.7	NEW
G321.93−0.00	15 19 41.1	-57 17 55	16.3	-38.6	2.2	-41.3	-34.5	NEW
G323.74−0.26	15 31 45.0	-56 30 33	11.3	-49.6	1.7	-52.7	-47.8	38
G324.18+0.41	15 31 36.1	-55 42 35	11.7	-56.6	1.1			NEW
G324.20+0.13	15 32 51.8	-55 55 57	82.9	-76.7	1.5	-91.8	-65.4	9
G325.63+0.29	15 40 20.8	-54 57 17	21.9	14.8	0.9			NEW
G326.06−0.14	15 44 32.5	-55 02 41	6.8	-75.0	2.6	-81.1	-70.4	NEW
G326.45+0.33	15 44 41.1	-54 25 45	6.2	-71.6	0.6			NEW
G326.48−0.37	15 47 48.0	-54 57 57	4.9	-51.6	1.0			NEW
G326.48+0.38	15 44 38.6	-54 22 50	67.9	-82.4	0.9	-85.7	-81.3	NEW, 48 - AGB star
G326.56+0.07	15 46 24.0	-54 34 21	10.3	1.9	1.0			NEW
G326.78−0.23	15 48 53.9	-54 40 11	93.9	-66.7	0.8	-70.9	-63.0	2
G327.40+0.45	15 49 17.7	-53 45 06	135.0	-80.2	1.0	-85.0	-75.8	9
G327.41−0.07	15 51 32.1	-54 08 56	9.3	-70.8	2.0	-95.5	-65.9	NEW, 30 - OH/IR star
G327.59−0.38	15 53 50.8	-54 16 18	24.3	-71.7	1.9			NEW
G327.65−0.38	15 54 09.2	-54 14 05	9.7	-73.1	2.2			NEW
G328.26−0.41	15 57 28.3	-53 52 10	11.9	-39.7	1.1			NEW
G328.31+0.43	15 54 06.1	-53 11 31	138.3	-94.7	1.1			9
G328.94−0.12	15 59 42.0	-53 12 18	5.5	-41.3	3.2			NEW
G328.99−0.43	16 01 20.5	-53 24 39	80.4	-84.9	1.5	-91.6	-82.1	NEW
G329.04−0.20	16 00 34.4	-53 12 07	4.2	-51.1	2.0	-55.9	-34.7	46
G329.09+0.42	15 58 09.5	-52 42 03	2.7	-55.0	3.5			NEW
G329.18−0.31	16 01 45.7	-53 11 26	171.1	-49.6	1.5	-128.4	-33.6	9
G329.21+0.44	15 58 38.4	-52 36 22	11.0	-106.1	2.1	-116.3	-102.3	NEW
G329.41+0.05	16 01 19.7	-52 46 22	28.2	-87.8	0.8			NEW, 29 - Carbon star
G329.41−0.45	16 03 30.9	-53 08 56	72.6	-75.6	1.3	-77.0	-68.3	9
G329.43−0.16	16 02 21.5	-52 54 47	12.4	-73.3	0.7	-103.9	-71.3	2
G329.53+0.09	16 01 43.4	-52 39 54	13.0	-91.7	0.8			NEW
G329.57−0.50	16 04 32.4	-53 04 36	4.2	-64.9	3.2	-67.8	-57.5	NEW
G329.63+0.14	16 02 00.2	-52 33 41	13.5	-89.5	1.7	-106.3	-87.2	2
G330.14−0.38	16 06 49.5	-52 36 38	5.8	-0.4	2.8			NEW
G330.29−0.39	16 07 37.2	-52 30 53	92.9	-78.8	1.0	-154.0	57.0	NEW
G330.47+0.03	16 06 35.9	-52 05 13	6.7	-58.0	0.8	-68.9	-40.5	NEW
G330.72+0.17	16 07 11.6	-51 48 46	50.3	70.3	0.5			NEW
G330.78+0.40	16 06 32.2	-51 36 11	3.0	-71.5	0.6	-81.4	-35.5	NEW
G330.85−0.43	16 10 27.5	-52 10 03	2.2	-33.6	1.2	-34.3	-26.2	NEW
G330.88−0.36	16 10 19.4	-52 05 59	90.6	-23.2	1.1	-109.9	-21.0	25
G330.95−0.18	16 09 51.9	-51 54 51	563.8	-91.5	2.8	-202.1	-66.5	42
G331.13−0.24	16 10 58.8	-51 50 12	165.4	-96.4	2.8	-115.0	-73.3	9
G331.14+0.16	16 09 14.9	-51 32 24	26.4	-76.0	1.8	-84.9	-73.9	NEW
G331.28−0.19	16 11 25.4	-51 41 51	120.3	-94.6	1.7	-104.8	-79.5	39
G331.44−0.18	16 12 11.3	-51 35 03	82.7	-88.5	1.5	-101.2	-83.6	2
G331.51−0.10	16 12 08.3	-51 28 30	927.3	-89.5	5.0	-164.5	-24.3	42
G331.55−0.12	16 12 25.6	-51 27 32	30.9	-101.5	1.2	-106.5	-84.0	9
G331.67+0.12	16 11 55.9	-51 12 39	7.5	-74.4	0.8	-76.4	-71.1	NEW
G331.75−0.32	16 14 16.1	-51 28 17	11.2	-34.1	4.8	-41.8	-18.5	NEW
G331.86+0.06	16 13 03.9	-51 07 10	7.9	-84.2	0.7			NEW
G331.97−0.24	16 14 53.5	-51 15 41	39.0	-86.3	1.0			NEW
G332.00−0.05	16 14 12.7	-51 06 22	3.2	-101.5	1.1	-102.4	-88.2	NEW
G332.09−0.42	16 16 15.1	-51 18 15	8.8	-59.4	0.6	-63.6	-52.4	2
G332.29−0.09	16 15 44.1	-50 55 52	69.5	-47.5	1.1	-52.6	-41.3	2
G332.33+0.18	16 14 41.2	-50 42 37	4.3	-47.6	0.6			NEW
G332.39−0.09	16 16 11.8	-50 51 56	4.2	-111.0	0.6			NEW

Table 2 – *continued ...*

Source Name	RA (J2000) (h m s)	Dec (J2000) (° ′ ″)	Strongest Maser Spot			Velocity Range		Comments[1]
			Peak Flux Density (Jy)	Velocity (km s^{-1})	FWHM (km s^{-1})	Min (km s^{-1})	Max	
G332.61−0.15	16 17 24.7	-50 45 18	4.7	-26.7	0.9	-29.8	-24.1	2
G333.00−0.43	16 20 24.9	-50 40 37	11.7	-110.4	2.0	-147.0	-93.8	40
G333.03−0.45	16 20 37.2	-50 40 27	5.0	-60.1	1.8	-61.6	-51.0	40
G333.06−0.48	16 20 55.9	-50 40 38	4.4	1.3	0.8	-10.9	2.8	47
G333.06−0.10	16 19 15.1	-50 24 20	8.8	-37.5	1.3	-49.4	-32.2	NEW
G333.12−0.43	16 20 59.3	-50 35 48	114.0	-56.4	1.5	-123.6	-43.9	42
G333.23−0.06	16 19 49.8	-50 15 10	516.9	-87.3	2.8	-94.0	-83.0	41
G333.31+0.11	16 19 28.1	-50 04 37	25.0	-45.3	1.7	-50.1	-42.0	2
G333.37−0.20	16 21 04.9	-50 15 26	4.6	-58.5	0.7	-63.2	-57.1	NEW
G333.46−0.16	16 21 18.3	-50 09 40	5.0	-42.8	1.8	-45.9	-41.1	2
G333.61−0.21	16 22 10.4	-50 05 54	268.7	-51.5	1.2	-53.3	-14.7	42
G333.63−0.36	16 22 56.9	-50 11 01	4.7	-71.1	1.3			NEW
G334.21+0.09	16 23 28.0	-49 27 15	17.4	-63.2	1.2	-65.7	-60.8	NEW
G334.39−0.18	16 25 26.0	-49 30 42	5.9	-123.8	2.6			NEW
G334.68+0.13	16 25 17.7	-49 05 33	9.0	-94.4	0.9	-106.0	-85.2	NEW
G334.94−0.34	16 28 31.4	-49 13 58	6.0	-35.7	1.3			NEW
G335.08−0.42	16 29 25.6	-49 11 28	36.3	-90.9	2.0	-92.7	-35.2	2
G335.23−0.33	16 29 41.6	-49 01 08	3.1	-52.3	2.4	-53.5	-31.8	NEW
G335.29−0.13	16 29 01.2	-48 49 56	2.0	-49.2	0.9			NEW
G335.43−0.24	16 30 07.0	-48 48 18	23.2	-40.8	1.0	-43.1	-39.7	NEW
G335.59−0.29	16 30 58.4	-48 43 36	34.7	-45.4	1.2	-60.6	-27.2	2
G335.70+0.20	16 29 17.2	-48 18 43	45.3	-45.3	0.7	-57.6	-44.4	2
G335.79+0.18	16 29 46.8	-48 15 42	39.0	-63.8	1.0	-91.1	-47.8	9
G336.13+0.26	16 30 47.6	-47 57 23	20.3	-46.6	1.1	-68.1	-28.0	NEW
G336.25−0.49	16 34 36.6	-48 22 56	4.8	-57.5	2.9			NEW
G336.50−0.26	16 34 36.0	-48 02 18	28.4	-24.9	1.0			NEW
G336.53−0.18	16 34 21.7	-47 57 34	3.0	-88.9	3.1			NEW
G336.83−0.38	16 36 26.5	-47 52 28	8.8	-20.1	1.4			2
G336.87+0.01	16 34 54.8	-47 35 28	6.7	-67.7	0.8			2
G336.88+0.01	16 34 58.4	-47 34 53	6.8	-72.5	0.7			2
G336.96−0.22	16 36 16.6	-47 40 45	5.4	-56.7	0.9			NEW
G337.00−0.03	16 35 34.9	-47 30 50	254.4	-120.3	1.5	-130.1	-112.0	25
G337.00−0.33	16 36 53.9	-47 42 57	55.5	-33.2	1.0	-49.7	-30.5	NEW
G337.13−0.07	16 36 15.8	-47 26 59	7.5	-61.3	0.9			NEW
G337.17−0.03	16 36 17.1	-47 23 32	15.4	-67.1	2.0			NEW
G337.21+0.12	16 35 47.5	-47 16 02	25.1	-71.8	5.9	-75.2	-65.8	NEW
G337.36+0.01	16 36 51.9	-47 13 39	5.3	-99.7	1.5			NEW
G337.40−0.40	16 38 49.2	-47 27 55	166.3	-40.6	0.9	-41.6	-37.0	25
G337.42−0.16	16 37 49.7	-47 17 40	166.0	-25.0	0.8	-26.1	-19.3	NEW
G337.62−0.06	16 38 10.4	-47 04 41	15.5	-49.7	1.3	-59.0	-45.1	9
G337.64+0.15	16 37 21.1	-46 55 39	3.5	-150.6	2.4			2
G337.72−0.06	16 38 32.9	-47 00 14	40.1	-52.6	1.4	-127.0	-34.2	9
G337.72+0.08	16 37 57.7	-46 54 21	33.9	-74.0	1.1	-143.2	25.2	NEW
G337.87+0.27	16 37 43.6	-46 40 27	100.6	-43.9	1.2	-82.5	-41.7	25
G337.88−0.11	16 39 26.7	-46 54 55	1.7	-49.8	2.9			NEW
G337.92−0.48	16 41 12.1	-47 07 57	677.2	-36.5	0.5	-68.5	-27.5	42
G338.00+0.13	16 38 50.0	-46 39 58	12.3	-37.0	3.4	-51.4	-33.9	9
G338.00−0.13	16 39 59.8	-46 50 38	5.5	-62.6	2.7	-65.7	-44.5	NEW
G338.17−0.07	16 40 20.9	-46 40 26	4.7	-57.7	1.0			NEW
G338.28−0.19	16 41 20.5	-46 40 11	5.0	-90.7	1.0	-92.1	-87.5	NEW
G338.29+0.12	16 40 02.0	-46 27 32	16.2	-38.7	1.2	-75.7	-33.6	NEW
G338.39−0.01	16 40 57.7	-46 28 01	63.2	-46.1	1.0			NEW
G338.39+0.16	16 40 14.2	-46 21 23	1.4	-29.1	3.2	-37.3	-23.2	NEW
G338.44+0.06	16 40 49.1	-46 23 11	4.7	-41.8	1.4			NEW
G338.47−0.25	16 42 18.1	-46 34 11	25.7	-52.9	0.7			2
G338.48+0.29	16 39 58.8	-46 12 21	16.2	-53.3	1.5			2
G338.50+0.05	16 41 07.2	-46 20 49	18.5	-41.3	1.5			NEW
G338.58+0.11	16 41 09.3	-46 15 08	10.8	-76.4	1.7			2
G338.68−0.08	16 42 24.2	-46 17 52	1.8	-22.1	1.6			2
G339.06+0.15	16 42 50.3	-45 51 38	10.5	-82.0	1.3	-90.2	-80.4	NEW

Table 2 – *continued ...*

Source Name	RA (J2000) (h m s)	Dec (J2000) (° ′ ″)	Peak Flux Density (Jy)	Velocity (km s^{-1})	FWHM (km s^{-1})	Min	Max	Comments[1]
			Strongest Maser Spot			Velocity Range (km s^{-1})		
G339.16−0.29	16 45 06.1	-46 04 09	3.1	-19.7	1.1			NEW
G339.20−0.02	16 44 05.8	-45 51 46	10.5	-14.6	0.7			NEW
G339.48+0.18	16 44 15.7	-45 31 26	2.9	-90.9	0.8			NEW
G339.52+0.27	16 44 01.2	-45 25 55	2.8	-14.5	0.7	-30.7	-13.7	NEW
G339.54−0.42	16 47 05.4	-45 52 11	1.2	-48.4	5.7			NEW
G339.59−0.14	16 46 02.7	-45 38 50	11.7	-33.2	1.2	-38.3	-24.6	9
G339.62−0.13	16 46 07.7	-45 36 59	238.9	-33.3	0.9	-38.4	-26.9	9
G339.75+0.10	16 45 37.0	-45 22 30	1.9	-77.9	4.4			NEW
G339.92−0.09	16 47 03.8	-45 21 38	6.0	-57.0	1.1			NEW
G340.05−0.24	16 48 12.5	-45 21 52	69.1	-55.2	2.0	-57.1	-46.4	9
G340.12−0.02	16 47 28.7	-45 10 05	69.9	-125.3	1.7			NEW
G340.13−0.18	16 48 15.6	-45 15 44	4.1	-4.7	1.7			NEW
G340.23−0.37	16 49 25.6	-45 18 14	52.0	-54.6	0.9			NEW
G340.25−0.04	16 48 04.4	-45 04 58	7.2	-127.6	1.5			NEW
G340.28−0.21	16 48 53.1	-45 10 14	10.7	-48.2	1.0	-49.0	-14.2	NEW
G340.29−0.03	16 48 11.2	-45 02 41	3.5	-114.3	3.4	-117.2	-111.7	NEW
G341.13−0.38	16 52 40.5	-44 37 23	11.0	-40.7	0.7			NEW
G341.22−0.21	16 52 16.7	-44 26 45	86.4	-40.9	1.0	-49.8	-37.9	3
G341.28+0.36	16 50 04.8	-44 02 03	10.0	-153.4	1.6	-157.6	-119.4	NEW
G341.31+0.19	16 50 52.8	-44 07 16	5.9	-110.6	1.8	-119.9	-103.5	NEW
G341.67+0.09	16 52 34.8	-43 54 28	7.3	-19.6	1.3			NEW
G341.99+0.26	16 53 00.3	-43 33 07	7.4	-38.1	1.1	-46.1	-19.8	39
G342.09+0.42	16 52 40.8	-43 22 23	34.8	-162.1	4.7			NEW
G342.33+0.10	16 54 50.6	-43 23 34	6.7	-97.5	1.6	-98.4	-92.4	NEW
G342.37+0.14	16 54 48.5	-43 20 01	8.1	-5.9	0.8			NEW
G342.47+0.20	16 54 55.9	-43 12 50	12.5	-50.5	0.7	-50.3	-31.0	NEW
G342.63−0.09	16 56 42.0	-43 16 46	3.3	-12.4	1.2			NEW
G343.13−0.06	16 58 16.4	-42 52 08	44.0	-19.8	0.8	-43.1	-14.8	9
G343.19−0.37	16 59 49.3	-43 00 26	3.1	-133.5	2.6	-135.7	-106.4	NEW
G343.48−0.06	16 59 28.4	-42 35 12	5.2	-33.3	1.4			NEW
G343.50−0.00	16 59 17.5	-42 32 20	21.9	-81.8	0.8			NEW
G343.50−0.06	16 59 32.3	-42 34 29	3.5	-34.3	1.0			NEW
G343.53−0.02	16 59 26.6	-42 31 45	11.0	-83.1	1.5			NEW
G343.69−0.02	16 59 59.7	-42 23 47	27.5	-36.0	1.2	-51.6	-31.6	NEW
G343.72−0.18	17 00 47.4	-42 28 47	13.8	36.3	1.2			NEW
G343.73−0.11	17 00 31.6	-42 25 13	20.5	-32.5	0.8			NEW
G343.75−0.15	17 00 45.3	-42 25 58	36.1	-23.5	0.9	-61.2	-22.1	NEW
G343.81+0.16	16 59 38.7	-42 11 54	7.6	22.2	1.2			NEW
G344.03−0.11	17 01 29.7	-42 11 26	78.7	-52.1	3.1	-60.2	-42.1	NEW
G344.30+0.16	17 01 16.1	-41 48 35	68.0	-30.2	5.5			NEW
G344.58−0.02	17 02 56.6	-41 42 13	1266.3	-4.1	1.5	-19.0	8.8	3
G344.65−0.22	17 04 00.3	-41 45 40	9.3	-60.2	1.3			NEW
G344.78−0.25	17 04 34.9	-41 40 29	4.6	-18.3	1.0			NEW
G344.89+0.12	17 03 23.0	-41 22 01	15.0	-28.5	1.4	-37.6	-25.1	NEW, 49 - S Star
G344.93+0.02	17 03 56.6	-41 23 41	8.3	-22.6	3.2	-24.9	-18.0	50 - Mira variable
G345.13−0.16	17 05 17.9	-41 20 54	19.3	-25.1	1.3	-27.3	-19.0	NEW
G345.25−0.03	17 05 08.2	-41 10 06	16.4	-23.6	1.4			NEW
G345.43−0.06	17 05 51.8	-41 02 33	54.6	-14.3	1.0	-28.5	-11.2	2
G345.44+0.21	17 04 46.2	-40 52 28	10.9	-16.6	1.5	-20.7	1.1	NEW
G345.50+0.36	17 04 19.6	-40 44 14	4.1	-19.7	0.5	-28.8	-12.0	41
G345.58−0.02	17 06 10.2	-40 53 53	5.8	-8.8	1.7			NEW
G345.65+0.02	17 06 14.4	-40 49 27	48.4	-11.3	3.8	-19.9	-0.4	39
G345.69−0.08	17 06 45.7	-40 50 46	297.0	-6.6	3.6	-13.9	87.6	42
G345.80−0.34	17 08 14.1	-40 55 11	3.6	-94.6	1.7			NEW
G345.83−0.05	17 07 04.7	-40 43 29	5.2	-6.9	0.7			NEW
G345.91−0.05	17 07 20.5	-40 39 30	2.7	-125.5	0.9			NEW
G345.98−0.01	17 07 22.6	-40 34 46	13.3	-77.5	1.3			NEW
G346.18−0.08	17 08 18.9	-40 27 11	7.3	-14.3	0.7			NEW
G346.18+0.34	17 06 34.1	-40 12 13	4.1	3.0	1.2			NEW
G346.47−0.23	17 09 52.2	-40 19 10	2.9	-76.3	2.6			NEW
G346.52+0.11	17 08 35.6	-40 04 34	6.2	3.2	1.9			2

Table 2 – *continued ...*

Source Name	RA (J2000) (h m s)	Dec (J2000) (° ′ ″)	Strongest Maser Spot			Velocity Range		Comments[1]
			Peak Flux Density (Jy)	Velocity (km s^{-1})	FWHM (km s^{-1})	Min (km s^{-1})	Max	
G346.53−0.12	17 09 33.8	-40 12 14	11.0	-47.4	0.6			NEW
G347.06+0.00	17 10 43.6	-39 42 17	3.7	-9.7	1.9			NEW
G347.23+0.02	17 11 10.0	-39 33 39	6.8	-77.8	1.2	-89.5	-73.5	NEW
G347.30+0.13	17 10 54.7	-39 25 54	42.3	-82.6	2.4	-98.4	-75.9	46
G347.32+0.02	17 11 26.9	-39 29 12	3.2	-8.5	1.1			NEW
G347.63+0.16	17 11 48.0	-39 09 18	15.0	-65.2	1.1	-127.9	-62.8	3
G347.63+0.22	17 11 34.9	-39 06 46	9.0	-90.2	1.7			51
G347.89−0.28	17 14 27.1	-39 11 52	4.9	-91.2	4.3	-94.4	-78.5	NEW
G348.18+0.48	17 12 06.9	-38 31 07	80.7	-1.4	0.7	-20.9	-0.8	39
G348.29+0.43	17 12 40.4	-38 27 12	5.2	-2.0	0.9			NEW
G348.32−0.18	17 15 16.6	-38 47 23	6.4	-100.8	1.4	-111.8	-97.2	NEW
G348.83+0.23	17 15 09.3	-38 08 11	3.5	-186.6	2.8			NEW
G348.89−0.18	17 17 01.0	-38 19 34	29.9	10.5	0.7			3
G349.10+0.11	17 16 24.5	-37 59 31	27.0	-79.5	2.4	-83.2	-69.8	25
G349.72+0.13	17 18 10.3	-37 28 14	149.6	17.9	2.7	11.6	22.5	NEW
G349.80+0.11	17 18 27.8	-37 25 06	107.5	-60.6	1.0			NEW
G350.11+0.09	17 19 25.9	-37 10 25	28.4	-72.9	4.3	-76.5	-27.8	3
G350.42−0.06	17 20 55.9	-37 00 24	62.4	-36.1	0.9	-37.0	-21.4	NEW
G350.53−0.34	17 22 24.5	-37 04 40	5.3	-17.3	0.7			NEW
G350.69−0.48	17 23 27.7	-37 01 15	60.3	-14.2	0.5			NEW
G350.88−0.29	17 23 11.6	-36 45 40	9.6	-53.9	1.0			NEW
G351.38+0.21	17 22 33.0	-36 04 00	5.3	7.3	0.7			NEW
G351.58−0.35	17 25 24.8	-36 12 34	137.9	-94.0	2.4	-96.0	-88.6	3
G351.62+0.18	17 23 21.6	-35 53 09	11.5	-42.2	0.8	-88.1	-9.7	NEW
G352.16+0.41	17 23 53.8	-35 18 18	158.7	-4.3	0.9			NEW
G352.21+0.10	17 25 17.3	-35 26 15	7.0	-28.2	0.7	-29.1	-21.6	NEW
G352.25−0.29	17 26 59.8	-35 37 16	6.4	-96.2	3.2	-98.6	-93.5	NEW
G352.55+0.20	17 25 49.2	-35 05 53	9.9	-52.2	0.6			NEW
G352.93+0.07	17 27 22.9	-34 51 40	8.9	-2.7	1.2			NEW, 52 - AGB star
G353.22−0.24	17 29 26.4	-34 47 30	85.7	-19.3	0.6	-22.7	-13.8	NEW
G353.26−0.24	17 29 33.0	-34 45 27	9.3	7.0	0.9			NEW
G353.39+0.43	17 27 11.0	-34 16 18	22.7	-40.6	4.4	-58.1	-10.1	NEW
G353.42−0.37	17 30 29.0	-34 41 38	10.9	-19.7	1.0			9
G353.82+0.32	17 28 47.4	-33 58 58	128.9	-70.5	2.6			NEW
G354.31−0.11	17 31 48.2	-33 48 25	13.7	9.0	0.8	6.5	17.9	NEW
G355.13−0.30	17 34 44.0	-33 13 07	106.4	224.8	1.0	4.3	227.6	NEW
G355.18−0.42	17 35 20.0	-33 14 23	21.1	0.2	1.8	-4.8	1.7	NEW
G355.34+0.15	17 33 28.1	-32 47 59	47.7	9.6	0.9			3
G355.79−0.18	17 35 55.6	-32 35 51	9.8	-2.1	0.7			NEW
G355.82+0.28	17 34 09.9	-32 19 43	14.2	-114.5	1.2	-117.0	-88.9	NEW
G355.93−0.34	17 36 57.4	-32 34 03	12.8	-49.7	1.7	-65.2	-42.8	NEW
G356.43+0.10	17 36 27.8	-31 55 07	2.8	-6.6	0.8			NEW
G356.47+0.01	17 36 54.7	-31 55 46	17.3	1.3	1.1			NEW
G356.55+0.08	17 36 49.4	-31 49 09	8.3	-19.0	2.7	-21.4	-15.0	NEW
G356.65−0.32	17 38 40.0	-31 56 57	11.7	4.6	3.1	-13.7	17.3	9
G357.57−0.32	17 40 57.6	-31 10 23	95.0	-8.4	1.9	-10.1	7.0	NEW
G357.57+0.07	17 39 27.5	-30 57 47	1.3	-48.0	4.6			NEW
G357.93−0.34	17 41 56.6	-30 52 56	15.4	1.4	0.8			NEW
G357.97−0.16	17 41 19.1	-30 44 58	130.7	-50.8	4.5	-70.6	92.6	46
G358.24+0.12	17 40 54.9	-30 22 16	94.0	-13.3	0.7	-15.6	-1.4	3
G358.30+0.08	17 41 11.5	-30 20 24	78.4	-9.2	1.1	-17.6	6.4	53
G358.39−0.48	17 43 38.9	-30 33 36	47.2	-0.6	2.7	-4.5	1.2	53
G358.47−0.38	17 43 26.1	-30 26 37	13.1	-4.7	1.1			NEW
G358.48−0.33	17 43 14.7	-30 23 58	10.0	0.3	1.0			NEW
G358.67−0.04	17 42 34.8	-30 05 39	60.9	-9.0	1.5	-21.1	-5.0	3
G358.88+0.04	17 42 46.5	-29 51 59	8.5	-17.6	2.0	-18.9	-10.3	NEW
G359.14+0.03	17 43 27.2	-29 39 23	498.7	-1.7	1.9	-13.2	24.6	54
G359.30+0.03	17 43 50.2	-29 30 50	20.1	0.9	1.5	-33.1	3.2	NEW
G359.42+0.07	17 43 57.1	-29 23 35	4.3	-5.3	1.5			NEW
G359.42+0.32	17 42 59.8	-29 15 49	4.4	9.5	0.8			NEW

Table 2 – *continued ...*

Source Name	RA (J2000) (h m s)	Dec (J2000) (° ′ ″)	Peak Flux Density (Jy)	Velocity (km s^{-1})	FWHM (km s^{-1})	Min (km s^{-1})	Max	Comments[1]
				Strongest Maser Spot		Velocity Range		
G359.44−0.10	17 44 41.1	-29 28 08	18.1	-58.4	2.2			3
G359.51−0.15	17 45 02.4	-29 25 59	5.6	7.2	0.8			53
G359.62−0.25	17 45 40.4	-29 23 35	106.4	-15.9	1.5	-25.5	11.6	3
G359.73−0.38	17 46 28.9	-29 21 56	42.2	-4.8	0.6	-14.8	-1.6	1
G359.94−0.15	17 46 03.4	-29 03 57	10.6	-18.7	1.7	-20.9	24.7	55
G359.97−0.46	17 47 21.6	-29 12 08	26.3	26.8	0.7	3.9	27.5	3
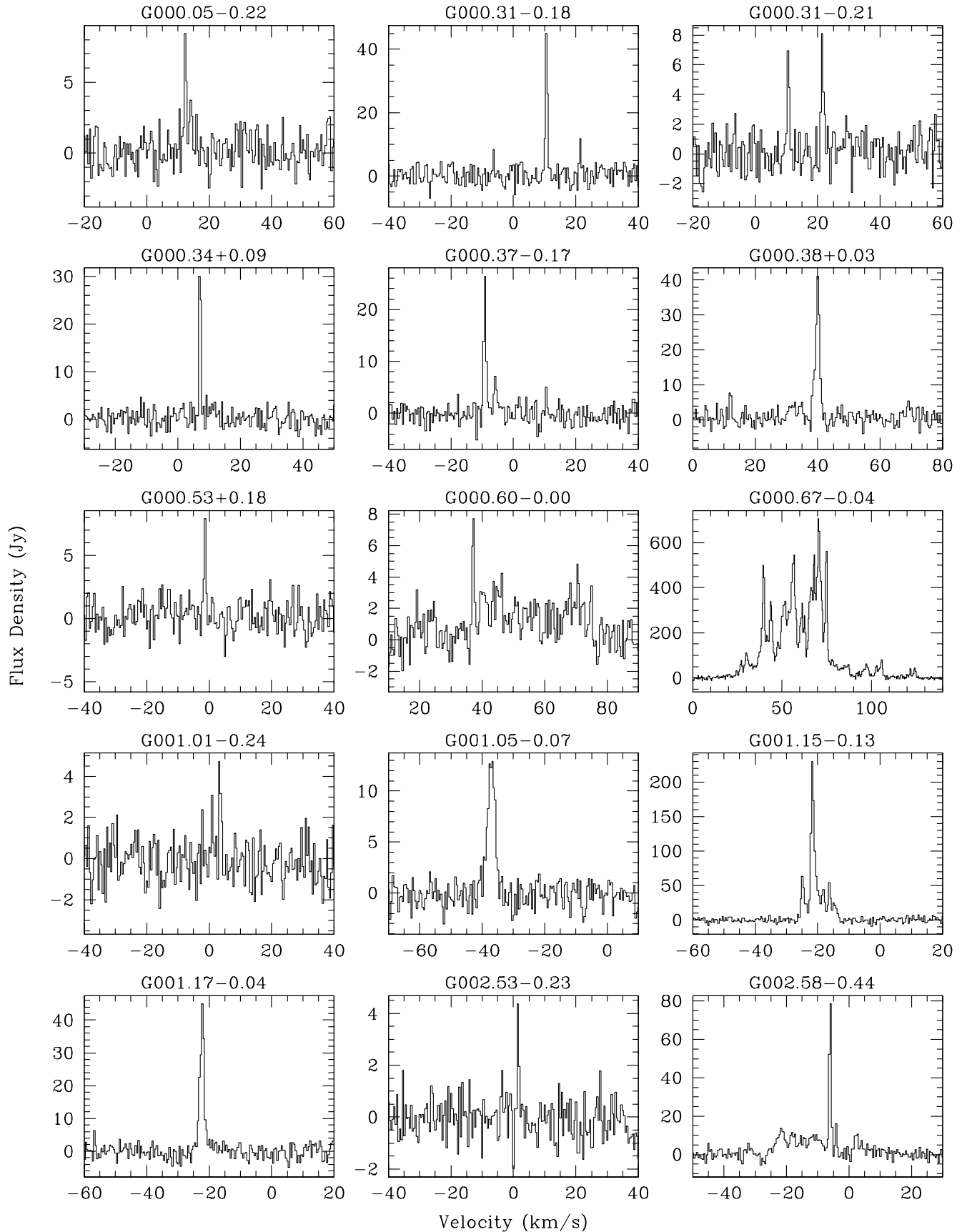
Figure 6. Spectra of water masers. The source name is given at the top of each panel.

Figure 6 – *continued ...*

Figure 6 – *continued* ...

G008.08+0.15

G008.20+0.13

G008.32−0.10

G008.41−0.30

G008.63−0.24

G008.67−0.36

G008.70−0.43

G008.73−0.39

G008.83−0.03

G008.93−0.02

G009.10−0.40

G009.62+0.19

G009.95+0.46

G009.98−0.03

G010.34−0.14

Flux Density (Jy)

Velocity (km/s)

Figure 6 – *continued ...*

Figure 6 – *continued ...*

Figure 6 – *continued ...*

Figure 6 – *continued ...*

Figure 6 – *continued ...*

Figure 6 – *continued ...*

Figure 6 – *continued ...*

Figure 6 – *continued ...*

Figure 6 – *continued …*

Figure 6 – *continued ...*

Figure 6 – *continued ...*

Figure 6 – *continued ...*

Figure 6 – *continued ...*

Figure 6 – *continued ...*

Figure 6 – *continued ...*

Figure 6 – *continued ...*

Figure 6 – *continued ...*

Figure 6 – *continued ...*

Figure 6 – *continued ...*

Figure 6 – *continued ...*

Figure 6 – *continued ...*

Figure 6 – *continued ...*

Figure 6 – *continued ...*

Figure 6 – *continued ...*

Figure 6 – *continued ...*

Figure 6 – *continued ...*

G342.09+0.42

G342.33+0.10

G342.37+0.14

G342.47+0.20

G342.63−0.09

G343.13−0.06

G343.19−0.37

G343.48−0.06

G343.50−0.00

G343.50−0.06

G343.53−0.02

G343.69−0.02

G343.72−0.18

G343.73−0.11

G343.75−0.15

Flux Density (Jy)

Velocity (km/s)
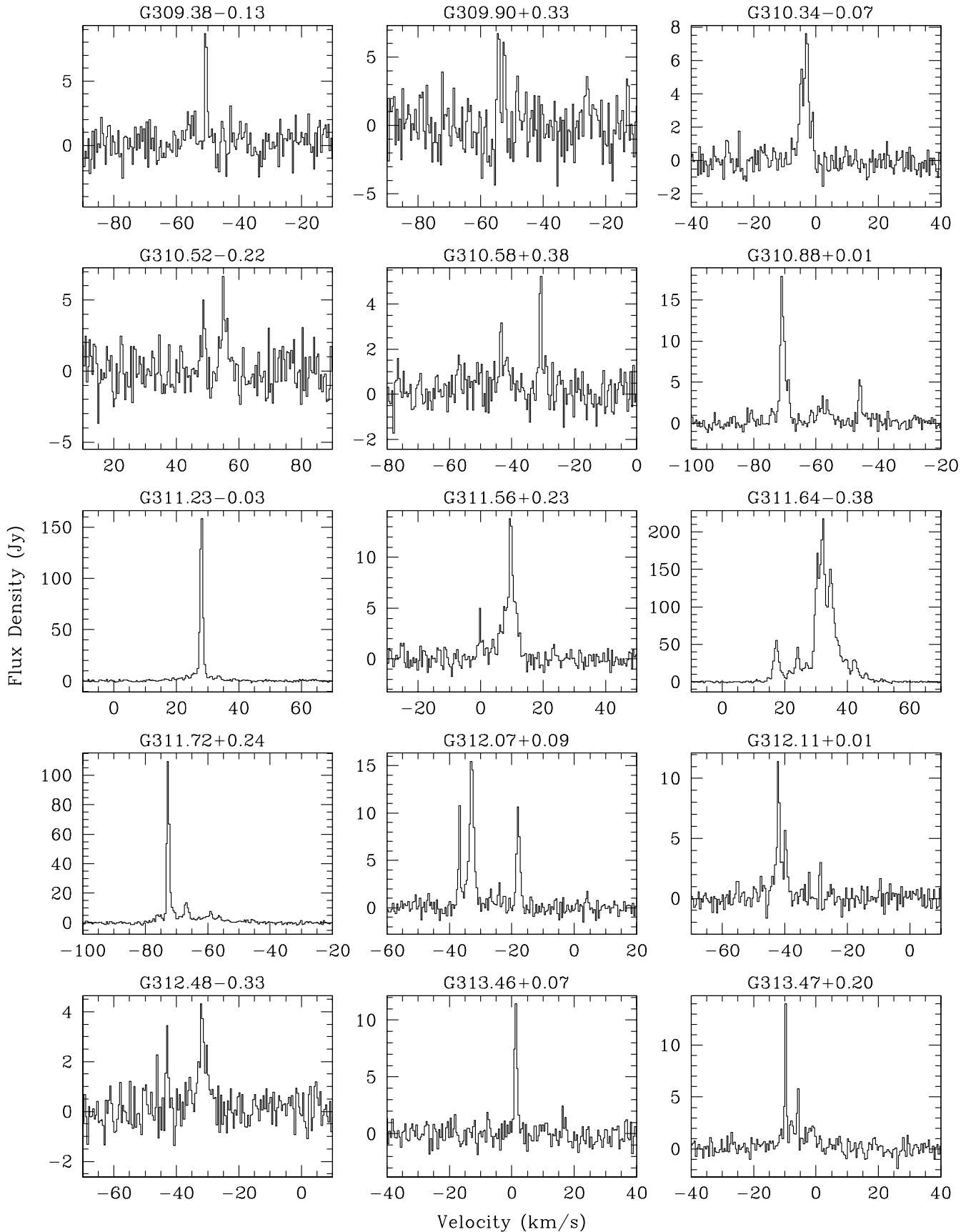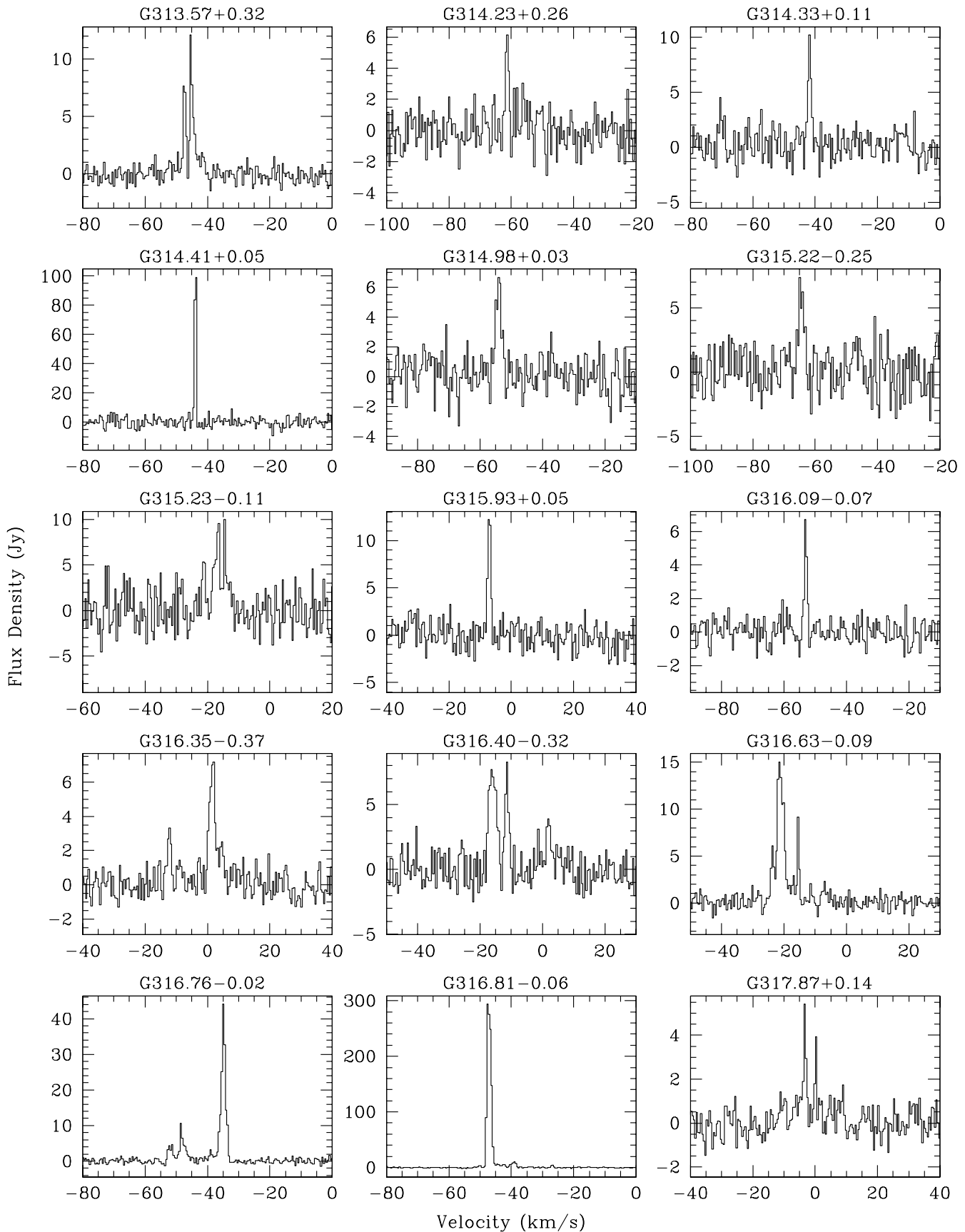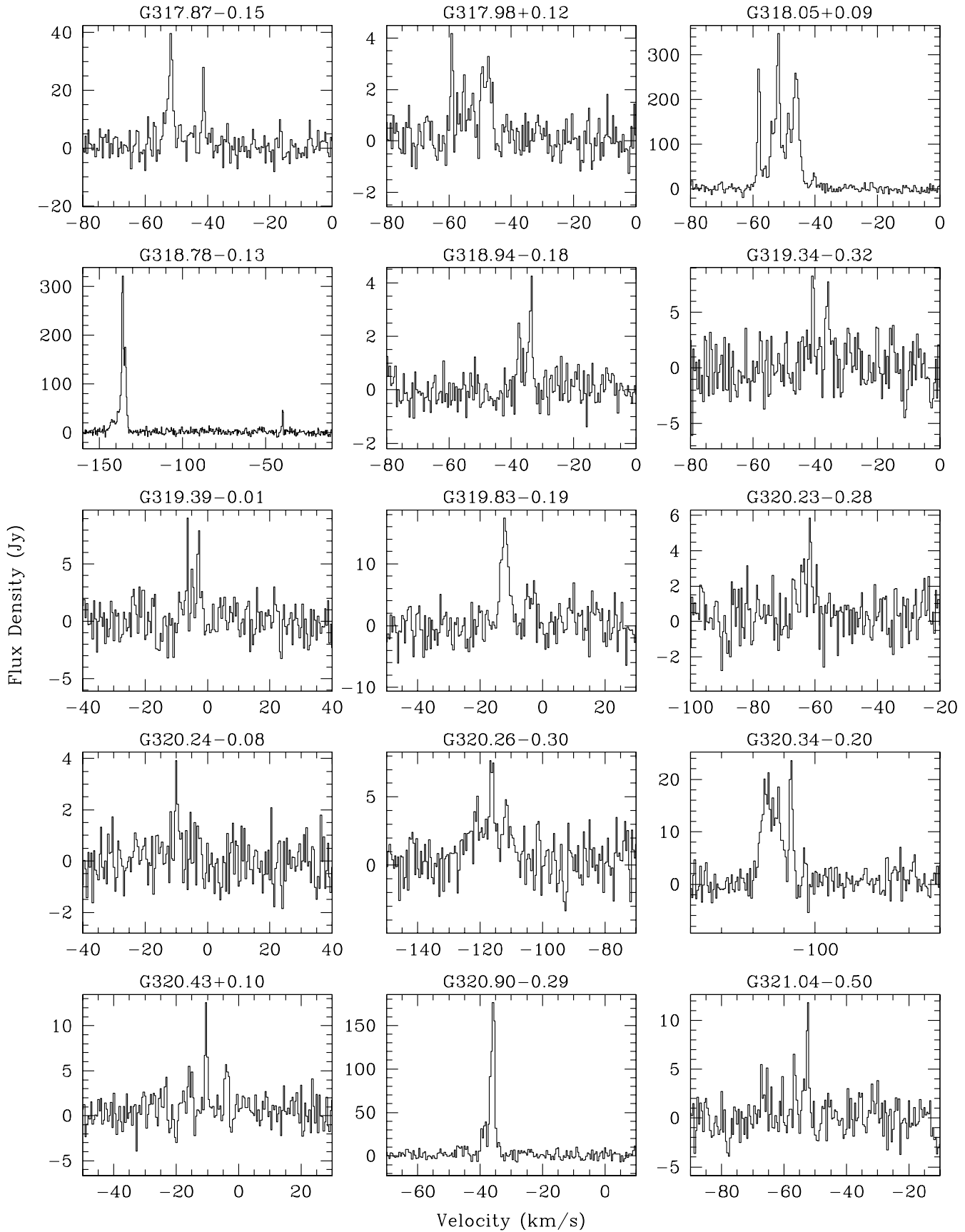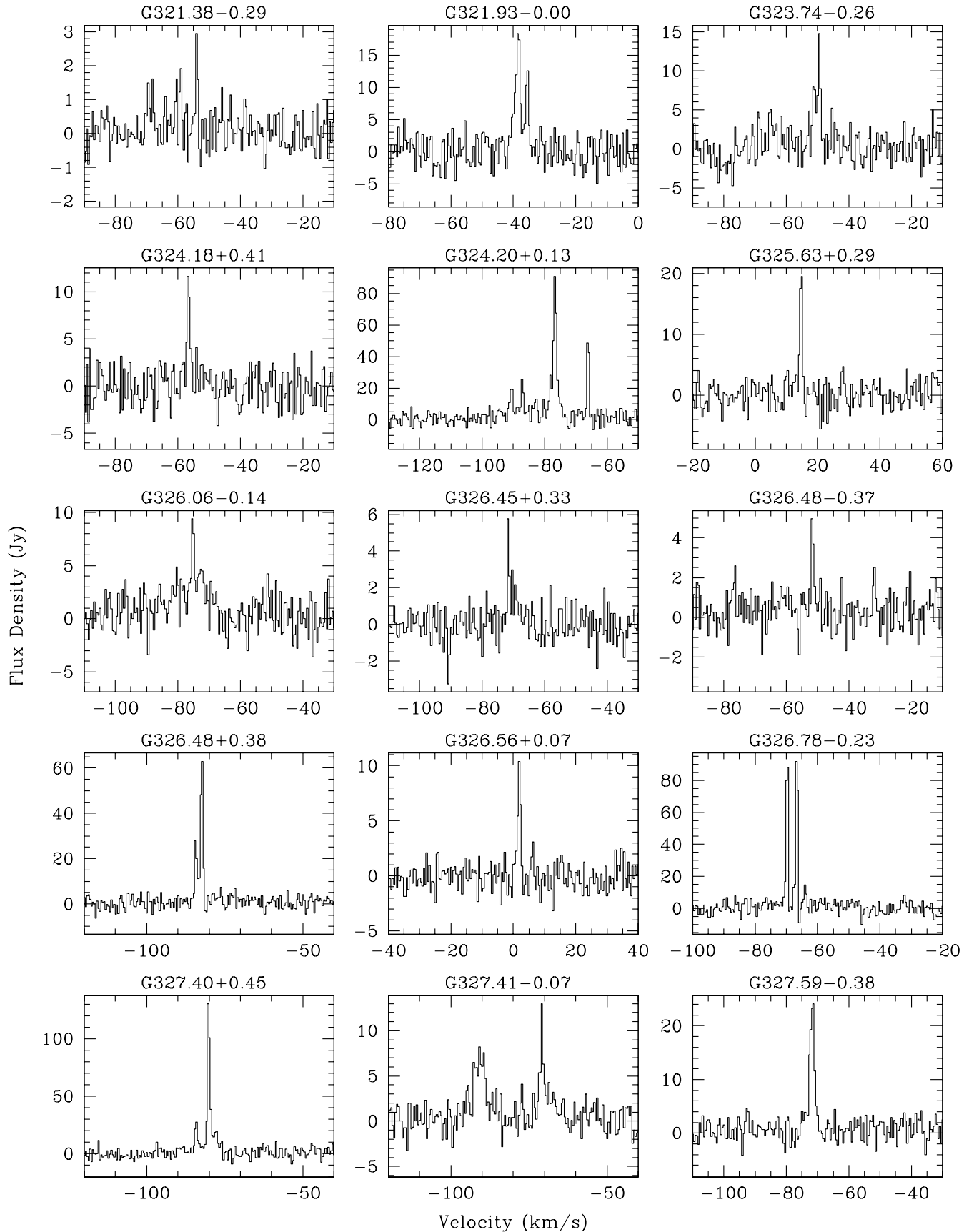
Figure 6 – *continued ...*

Figure 6 – *continued ...*

Figure 6 – *continued ...*

Figure 6 – *continued ...*

Figure 6 – *continued ...*

Figure 6 – *continued ...*

Figure 6 – *continued ...*

Figure 7. Distribution of H_2O maser velocity spreads for maser sites showing more than one maser spot. The majority of maser sites are confined to a velocity spread of less than $17 \, \text{km s}^{-1}$ and 90% of maser sites have a velocity spread of less than $50 \, \text{km s}^{-1}$.

There are 303 H_2O maser sites that show more than one peak in the maser spectrum (we refer to such single peaks in the spectrum as maser spots). Of these sites with more than one maser spot, the widest velocity distribution is exhibited by G9.10−0.40, over $351.3 \, \text{km s}^{-1}$. This maser site was previously reported by Walsh et al. (2009), based on HOPS data, and is a water fountain associated with a post-AGB star. Subsequent observations by Walsh et al. (2009) found maser emission over an even wider range of $398 \, \text{km s}^{-1}$.

In total, there are 14 maser sites with maser spots spread over a velocity range greater than $100 \, \text{km s}^{-1}$. The median velocity spread is $17 \, \text{km s}^{-1}$. The distribution of velocity spreads of maser sites with multiple maser spots can be seen in Figure 7. The Figure shows that the occurrence of maser sites with high velocity features is relatively rare, but there is a population of about 10% of maser sites with maser spots that span velocity ranges greater than $50 \, \text{km s}^{-1}$.

When comparing the line FWHM of maser spots, we find that G27.08+0.20 exhibits the widest FWHM of $13.3 \, \text{km s}^{-1}$. However, because maser sites usually consist of multiple peaks in the spectrum, it is likely that any single peak may comprise multiple unresolved components in the spectrum. This is likely to be the case for G27.08+0.20 whose H_2O maser emission is very weak and dominated by noise, possibly masking multiple components. The median line FWHM is $1.2 \, \text{km s}^{-1}$ and 90% of maser spots are no broader than $3.1 \, \text{km s}^{-1}$.

In Table 2, the last column indicates whether a maser site is coincident with the position and shows similar spectral features to the H_2O maser emission from a known evolved star. There are 15 maser sites so far associated with evolved stars. Due to the $2'$ beam of the Mopra observations, we await higher resolution observations to associate all masers

with a particular class of astrophysical object. There are certainly known evolved stars within $2.2'$ of H_2O masers which we have not yet associated because we cannot compare our H_2O maser spectrum to a previously published spectrum. We thus expect there to be more associations with evolved stars to be uncovered, but with the majority of maser sites associated with star forming regions. See §7.4 for further evidence that leads us to this expectation. We plan to conduct follow up observations of the maser sites with the ATCA, which will give us high positional accuracy, allowing us to identify the majority of maser sites with known astrophysical objects.

7   DISCUSSION

7.1   Noise measurements

We expect the noise level in our spectra to vary by about a factor of two because observations were made at a range of elevations and weather conditions, which gave rise to system temperature variations in the range 50 to 120 K. In order to determine the sensitivity limits of the water maser data, we measure the rms noise levels for each quarter-square-degree. This is done by taking a single channel from the data cube where no emission is expected (typically a channel at a velocity of $+250 \, \text{km s}^{-1}$ was used). Then the rms noise is measured for each quarter-square-degree using the MIRIAD task IMSTATS. We also checked the noise levels at different parts of each zoom band and found that the noise does not vary significantly within each zoom. This is done for each of the IFs containing H_2O maser, NH_3 (1,1), HCCCN (3–2) and H69α emission. These IFs were chosen because they contain the most important emission lines in the survey and because they sample close to the full range of frequencies observed in HOPS, from 19.6 GHz (H69α) to 27.3 GHz (HCCCN (3–2)).

Figure 8 shows histograms of the noise levels measured for each of the IFs. The rms noise levels are typically around 0.15 to 0.2 K in terms of main beam brightness temperature. We show the H_2O maser rms noise level in terms of Jy, as this is a more typical intensity scale used for masers (assuming $12.4 \, \text{Jy K}^{-1}$). For H_2O masers, we find the rms noise level is below 2 Jy for 95% of the survey and below 1.4 Jy for 50% of the survey. The full range of noise levels varies by a factor of 2.9, but we find that 87% of the H_2O maser observations are characterised by a rms noise level between 1 and 2 Jy.

We find that 90% of the rms noise levels in the IFs containing NH_3 (1,1), H69α and HCCCN (3–2) emission are between 0.12 and 0.24 K. Thus, we consider that the rms noise levels in the survey are well characterised by variation of a factor of two, but note that approximately 10% of the rms noise levels in the survey lie outside this range.

7.2 H_2O maser completeness limits

In order to estimate the completeness of the H_2O maser observations, we took a H_2O maser data cube, with a representative noise level of 1.5 Jy (rms), but without any identified H_2O masers. We injected fake signals into the spectrum, using the IMGEN task in MIRIAD, to mimic the typical characteristics of a real H_2O maser: a three-dimensional gaussian with the size of the beam in the spatial axes and line width
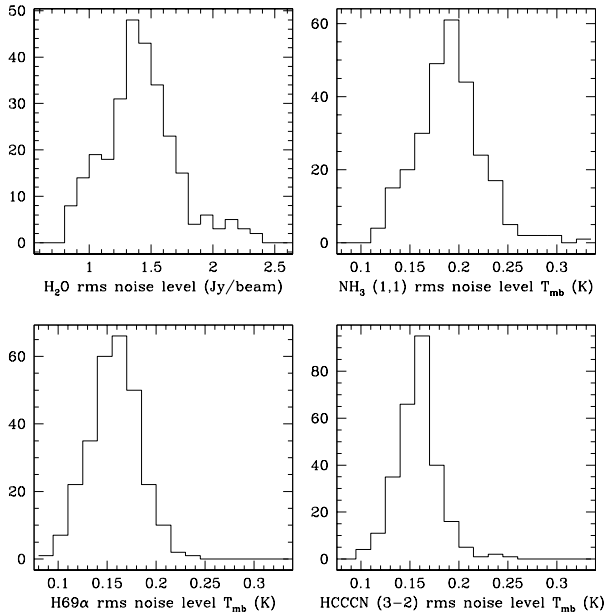
Figure 8. Histograms of rms noise levels. **Top-left** H$_2$O maser noise levels in units of Jy/beam, assuming a conversion factor of 12.4 Jy/K. **Top-right** NH$_3$ (1,1) rms noise levels in units of main beam brightness temperature. **Bottom-left** H69α radio recombination line rms noise levels in units of main beam brightness temperature. **Bottom-right** HCCCN (3–2) rms noise levels in units of main beam brightness temperature.

Figure 9. Distribution of H$_2$O maser peak flux densities, based on the strongest maser spot in each maser site. The histogram shows the distribution of detected masers, with error bars representing $\sqrt{N}$ statistics. The solid straight line is a power law fit to the distribution above the 100% completeness limit of 10 Jy, with slope -0.66. The dotted line represents the apparent turnover in the distribution due to the completeness limit. This dotted line is consistent with the histogram implying that we do not see a significant turnover in the population of H$_2$O maser flux densities.

the same as the median H$_2$O maser line width of $1.2\,\mathrm{km\,s^{-1}}$. The same data reduction routines and visualisation methods were used to identify the fake masers. In each test we used 100 fake masers and each test was repeated for four discrete input flux densities. We found the following successful recovery rate of fake masers in the data cube: at 11.1 Jy, we recovered 100% of the fake masers, at 8.4 Jy we recovered 98%, at 6.7 Jy we recovered 86% and at 5.5 Jy we recoved 50%. Therefore, we consider that for typical observing conditions, we are complete to about 10 Jy and 50% complete to about 5.5 Jy.

Figure 9 shows the distribution of peak flux densities of the strongest maser spot in each maser site. This figure shows that the number of masers sharply rises from the strongest masers down to about 5 Jy, The distribution above the 100% completeness limit (10 Jy) is well matched to a power law with slope -0.66 down to this point (the solid straight line in Figure 9). The dotted curve extending from the straight line indicates the expected numbers of masers, assuming that the real distribution of maser fluxes would follow the straight line extended to lower flux levels, together with the above completeness figures. The apparent turnover seen in the dotted line is consistent with the distribution of detected maser flux densities, shown by the histogram, given error bars that are based on $\sqrt{N}$ statistics. This means that although the distribution shows a peak of masers, this is likely due to the completeness limit of the survey and not due to an intrinsic turnover in the maser flux density population.

7.3   Other maser detections

Within the HOPS region we made occasional detections of other maser lines towards 11 regions. These include detections from the CH$_3$OH (J$_2$ – J$_1$) E series near 25 GHz and the previously unknown masing transition of CH$_3$OH at 23.444 GHz. The 23.444 GHz CH$_3$OH detection has been confirmed as a maser by Voronkov et al. (2011). In addition to this, we detected possible maser emission in the NH$_3$ inversion transitions (11,9), (8,6) and (3,3). Details of the NH$_3$ detections are given below.

7.3.1   NH$_3$ (11,9) and (8,6)

Emission in these two inversion transitions of NH$_3$ have previously been reported towards one position: NGC 6334 I (Walsh et al. 2007b) and confirmed as new masing transitions. We detect emission from both transitions in HOPS towards one new position: G19.61-0.23. Spectra of emission in the two transitions are shown in Figure 10. We also detect H$_2$O maser emission at this position, as detailed in Table 2 and shown in Figure 6. However, we note that the emission of the NH$_3$ transitions at approximately $55.5\,\mathrm{km\,s^{-1}}$ is on the edge of the extent of the H$_2$O maser emission and about $11\,\mathrm{km\,s^{-1}}$ offset from the strongest H$_2$O maser spot.

We cannot confirm that these two emission lines are due to masers with the current data, but the fact that the lines are typically narrow (1.5 and $1.1\,\mathrm{km\,s^{-1}}$ for (11,9) and (8,6), respectively) and that these transitions have only been
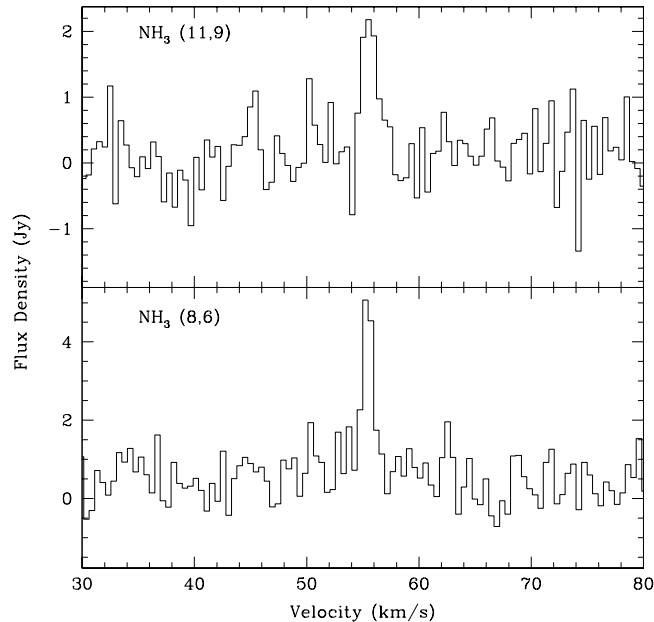
Figure 10. NH$_3$ emission spectra towards G19.61-0.23 in the (11,9) inversion transition (**top**) and (8,6) transition (**bottom**). Emission in the (11,9) transition has a peak flux density of 2.2 Jy, line velocity of 55.6 km s^{-1} and line FWHM of 1.5 km s^{-1}. Emission in the (8,6) transition has a peak flux density of 4.9 Jy, line velocity of 55.4 km s^{-1} and line FWHM of 1.1 km s^{-1}.

previously detected as masers, suggests that a maser origin is more likely than a thermal origin.

G19.61-0.23 is a well known region of high mass star formation in the Galaxy, containing OH (Caswell & Haynes 1983) and CH$_3$OH masers (Caswell et al. 1995; Walsh et al. 1998), including the rare 9.9 GHz CH$_3$OH maser (Voronkov et al. 2010), cold dust continuum emission (Walsh et al. 2003; Thompson et al. 2006), molecular line emission (Santangelo et al. 2010) and multiple ultracompact (UC) H$_{II}$ regions (Garay et al. 1998). Kolpak et al. (2003) determine a distance to G19.61-0.23 of 12.3 kpc, based on H$_I$ observations. It is surprising that one of only two known sources of emission in these NH$_3$ lines is at such a large distance. This suggests G19.61-0.23 may be an unusual region of maser activity in the Galaxy otherwise we would expect to detect other maser sites closer to us. Garay et al. (1998) concluded that in this region an ionisation front is driven by an expanding H$_{II}$ region into a molecular cloud. Together with the presence of the rare 9.9 GHz CH$_3$OH maser, which is known to trace strong shocks, it is possible that the NH$_3$ masers are created in the shock interface between H$_{II}$ region and molecular cloud.

7.3.2   NH$_3$ (3,3)

We find widespread thermal NH$_3$ (3,3) emission throughout the HOPS region. However, here we report on the possible detection of a maser in this transition. The possible maser is located at G23.33-0.30. The spectra of NH$_3$ (1,1), (2,2) and (3,3) emission at the position of G23.33-0.30 are shown in Figure 11.
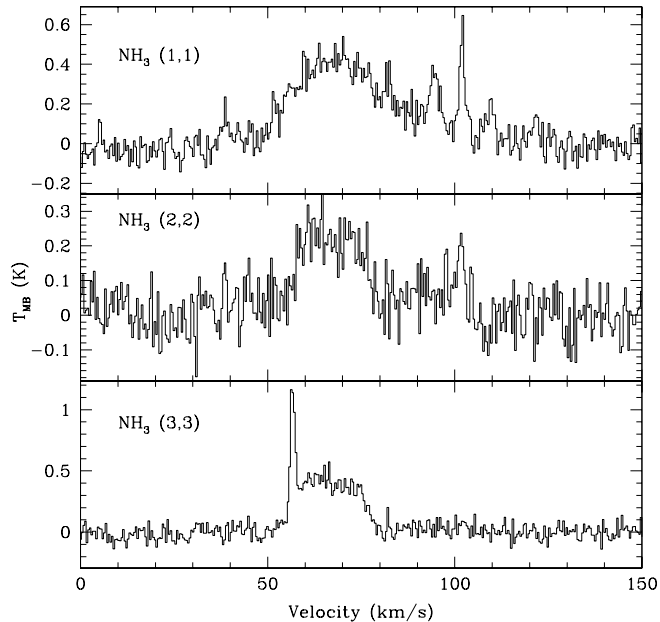
Figure 11. NH$_3$ emission spectra towards G23.33-0.30. (**Top**) NH$_3$ (1,1) emission showing a broad peak centred at approximately 70 km s^{-1} and a line FWHM of approximately 40 km s^{-1}. There is a second NH$_3$ (1,1) source centred at approximately 102 km s^{-1}, with line FWHM of 1.9 km s^{-1}. The second source also exhibits hyperfine structure. (**Middle**) NH$_3$ (2,2) emission also showing the two features identified in the (1,1) spectrum at a somewhat weaker level. (**Bottom**) NH$_3$ (3,3) emission showing a broad emission feature, as for the (1,1) and (2,2) spectra, with peak around 64 km s^{-1} and line FWHM approximately 20 km s^{-1}. A new narrow-lined feature is seen in the (3,3) spectrum at 56.7 km s^{-1}, with a line width of 1.2 km s^{-1}. This feature is suspected to be a maser.

We suspect that the narrow-lined emission peak at 56.7 km s^{-1} is a maser because this feature is not seen in either of the (1,1) or (2,2) spectra. It also shows an unusually narrow line FWHM of 1.2 km s^{-1}, ie. much narrower than the typical (1,1) and (2,2) thermal linewidths (Longmore et al. 2007). We await further observations to confirm, or otherwise, the maser nature of this emission feature, as it is not possible to conclude given the current data. The NH$_3$ (3,3) transition has previously been detected as a maser in DR 21(OH) (Mangum & Wooten 1994), W51 (Zhang & Ho 1995), NGC 6334 I (Kraemer & Jackson 1995) and G5.89-0.39 (Hunter et al. 2008). However, in all previous detections, the NH$_3$ (3,3) maser has never been seen stronger than 0.5 Jy. Our observations of the suspected maser in G23.33-0.30 give a peak flux density of 9.7 Jy above the NH$_3$ (3,3) thermal emission, which would make it the brightest NH$_3$ (3,3) maser known by over an order of magnitude.

G23.33-0.30 is associated with an infrared dark cloud (Perettero & Fuller 2009) and cold dust continuum source (Di Francesco et al. 2008). It is also associated with a Class II CH$_3$OH maser (Szymczak, Hrynek & Kus 2000), however, the CH$_3$OH maser emission is seen over a velocity range that covers between 63 and 76 km s^{-1} and does not overlap with the suspected NH$_3$ (3,3) maser. Based on the

possible associations, the suspected NH_3 (3,3) maser is likely to arise from a high mass star forming region, although the exact nature of any associations will almost certainly require higher spatial resolution observations to investigate the spatial coincidence of the NH_3 (3,3) emission and other features in this region.

7.4 H_2O maser Galactic latitude distribution

Figure 12 shows the Galactic latitude distribution for water masers detected in HOPS. The dashed line in Figure 12 shows a fitted Gaussian to the distribution, which has a peak at $-0.062°$ and FWHM of $0.60°$. The FWHM corresponds to a scale height of $0.5°$, which is slightly smaller than the scale height for UC H$_{II}$ regions of $0.6°$ (Wood & Churchwell 1989b) and slightly larger than the scale height found for Class II CH_3OH masers of $0.4°$ (Walsh et al. 1997). Both UC H$_{II}$ regions and Class II CH_3OH masers are reliable tracers of high mass star formation and their scale height appears to be the smallest known for any class of Galactic object. Since the H_2O masers appear to be as tightly constrained as the UC H$_{II}$ regions and the CH_3OH masers, we surmise that the majority of detected H_2O masers are likely drawn from the same population as regions of high mass star formation.

Given the fitted Gaussian to the Galactic latitude distribution, we can estimate the number of water masers that are detectable, but lie at Galactic latitudes outside the survey area, between Galactic longitudes of $290°$ and $30°$. This is done by integrating under the entire Gaussian curve and comparing this number to the 540 detected masers in the area under the curve between $-0.5°$ and $+0.5°$. We find that this analysis yields about 32 undetected maser sites, or 6%. We expect this number of undetected masers is a lower limit. This is because, as mentioned above, the Gaussian is dominated by maser sites associated with high mass star formation. But H_2O masers are known to also be associated with evolved stars, which have a larger scale height about the Galactic plane. Based on a 1612 MHz OH maser survey towards evolved stars (Sevenster et al. 1997), we estimate the scale height of evolved stars is $1.5°$. Therefore, we expect more detections of water masers at higher Galactic latitudes from evolved stars. Only 15 maser sites in our survey have been associated with evolved stars, with possibly some other maser sites yet to be associated. We estimate that probably no more than 10% of all detected masers will be associated with evolved stars, making them a minor contribution to the total number of masers. Assuming up to 10% of masers are associated with evolved stars, which have a scale height of $1.5°$, we estimate that no more than about 73 detectable masers lie in this region.

7.5 H_2O maser Galactic longitude distribution

Note that we have only considered the regions at greater Galactic latitudes, but within the same Galactic longitude range, as the survey area. This covers approximately 28% of all Galactic longitudes. If we assume the distribution of H_2O masers is symmetrical about the Galactic centre in Galactic longitude, then given there are 339 masers between $l = 290°$ and $0°$, we estimate there at least 680 masers between $l = 290°$ and $l = 70°$ and $|b| < 0.5°$. Based on the
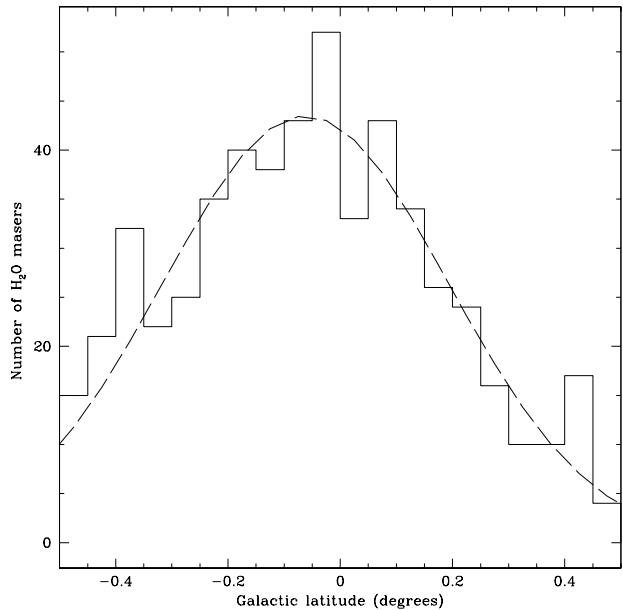

Figure 12. Galactic latitude distribution of H_2O masers detected in HOPS. The number of water masers is shown by the histogram and a fitted Gaussian to the distribution is shown as the dashed line. The fitted Gaussian has a peak at -0.062° and FWHM of 0.60°.

scale heights given above, we estimate that there are about 800 detectable masers at all Galactic latitudes, within this Galactic longitude range. Without knowing the true distribution of H_2O masers in the outer Galaxy, we cannot reliably extrapolate to the number of detectable masers in the entire Galaxy. However, we expect that the remaining 45% of the Galaxy will not contain as many detectable H_2O masers as the inner Galaxy, so we place an approximate upper limit of 1500 in the entire Galaxy. In conclusion, we estimate that there are between 800 and 1500 H_2O masers in the Galaxy that are detectable with a survey sensitivity comparable to HOPS.

Figure 13 shows the distribution of H_2O masers in Galactic longitude. There are three prominent concentrations of H_2O masers at approximately $310°$, $335°$ and $25°$. These positions in the Galaxy correspond to tangent points of Galactic spiral arms. Towards the Galactic centre, we do not find any peak in the number of H_2O masers, compared to other longitudes within $20°$ of the Galactic centre. This is somewhat surprising as the Galactic centre is very prominent in many spectral line tracers, such as NH_3, reported in Longmore et al. (*in preparation*). We will compare the positions of H_2O masers and dense molecular gas in future papers.

8   CONCLUSIONS

We have completed observations of 100 square degrees of the Galactic plane, using the Mopra radiotelescope in the 12 mm band, in a survey we call HOPS (the **H$_2$O** Southern Galactic **P**lane **S**urvey). Our observations concentrated
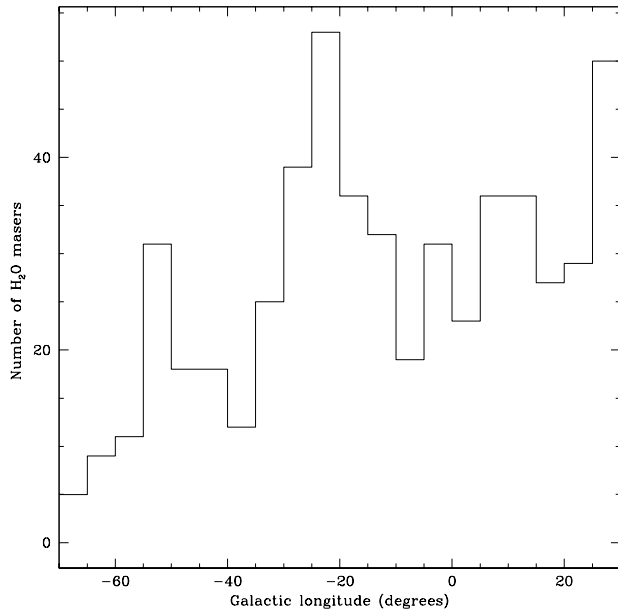
Figure 13. Galactic longitude distribution of H_2O masers detected in HOPS. Three peaks are seen at approximately $310°$, $335°$ and $25°$, which correspond to tangent points of the Galactic spiral arms. There is no prominent peak towards the Galactic centre.

on spectral line emission from the H_2O maser at $22.2\,GHz$, the NH_3 inversion transitions (1,1), (2,2), (3,3), (6,6) and (9,9), HCCCN (3–2), and radio recombination lines H69α and H62α. We have reported on the survey design, covering Galactic longitudes from $l = 290°$ to $l = 30°$ and Galactic latitudes $|b| < 0.5°$.

Within the survey region, we found 540 H_2O masers, of which 334 (62%) are new detections. We find maser peak flux densities ranging from 0.7 to $3933\,Jy$, with 62 masers (9%) over $100\,Jy$. We find maser spot velocities spread over ranges up to $351.3\,km\,s^{-1}$, with 14 maser sites showing spot velocities spread over at least $100\,km\,s^{-1}$. We estimate that at least 90% of the detected masers oucld be associated with high mass star formation, with the remainder being associated with evolved stars or low mass star formation. This is based on the number of known associations of H_2O masers and evolved stars in our survey (15) and the Galactic latitude distribution of the H_2O masers, which closely resembles the distribution of high mass star formation sites.

Our rms noise levels for the H_2O maser observations are between 1 and $2\,Jy$ for 87% of the survey, with 95% of the survey having an rms noise level below $2\,Jy$. We estimate that the survey is 98% complete down to a flux limit of about $8.4\,Jy$ and 50% complete down to about $5.5\,Jy$. We estimate that there are between 800 and 1500 H_2O masers in the Galaxy that are detectable in a survey with such completeness limits.

We detect possible masers in transitions of CH_3OH and NH_3. This includes the detection of NH_3 (11,9) and (8,6) emission towards G19.61-0.23. If these transitions are confirmed as masers, they will be only the second known examples of these transitions showing maser activity. We also

report possible maser emission in the NH_3 (3,3) line towards G23.33-0.30. If confirmed as a maser, it will be the strongest known maser in this line by at least an order of magnitude.

In Paper II (Purcell et al. 2011, *in preparation*) we present NH_3 (1,1) and (2,2) data, the source finding algorithm and thermal line fitting routines. Paper III (Longmore et al. 2011, *in preparation*) will detail properties of all other thermal lines detected in HOPS.

REFERENCES

Aikawa Y., Ohashi N., Inutsuka S., Herbst E., Takakuwa S., 2001, ApJ, 552, 639

Alksnis A., Balklavs A., Dzervitis U., Eglitis I., Paupers O., Pundure I., 2001, Balt A, 10, 1

Barlow M.J. et al., 1996, A&AL, 315, 341

Batchelor R.A., Caswell J.L., Goss W.M., Haynes R.F., Knowles S.H., Wellington K.J., 1980, AuJP, 33, 139

Benson P.J., Little-Marenin I.R., Woods T.C., Attridge J.M., Blais K.A., Rudolph D.B., Rubiera M.E., Keefe, H.L., 1990, ApJS, 74, 911

Benson P.J., Little-Marenin, I.R., 1996, ApJS, 106, 579

Bergin E.A., Alves J., Huard T., Lada C.J., 2002, ApJL, 570, 101

Bergin E.A., Langer, W.D., 1997, ApJ, 486, 316

Brand J. et al., 1994, A&AS, 103, 541

Braz M.A., Gregorio Hetem J.C., Scalise E.Jr., Monteiro Do Vale J.L., Gaylard, M., 1989, A&AS, 77, 465

Braz M.A., Scalise E.Jr., 1982, A&A, 107, 272

Breen S.L., Caswell J.L., Ellingsen S.P., Phillips, C.J., 2010, MNRAS, 406, 1487

Breen S.L. et al., 2007, MNRAS, 377, 491

Caselli P., Walmsley C.M., Tafalla M., Dore L., Myers, P.C., 1999, ApJL, 523, 165

Caswell J.L., Breen S.L., Ellingsen S.P., 2011, MNRAS, 410, 1283

Caswell J.L., Breen S.L., 2010, MNRAS, 407, 2599

Caswell J.L., Vaile R.A., Ellingsen S.P., Whiteoak J.B., Norris R.P., 1995, MNRAS, 272, 96

Caswell J.L., Batchelor R.A., Forster J.R., Wellington, K.J., 1989, AuJP, 42, 331

Caswell J.L., Haynes R.F., 1983, AuJP, 36, 417

Caswell J.L., Batchelor R.A., Forster J.R., Wellington, K.J., 1983, AuJP, 36, 401

Caswell J.L., Batchelor R.A., Forster J.R., Wellington, K.J., 1983, AuJP, 46, 443

Caswell J.L., Batchelor R.A., Goss W.M., Haynes R.F., Wellington, K.J., Yabsley D.E., Knowles S.H., Balister, M., 1976, PASA, 3, 61

Caswell J.L., Batchelor R.A., Haynes R.F., Huchtmeier, W.K., 1974, AuJP, 27, 417

Churchwell E., Walmsley C.M., Cesaroni, R., 1990, A&AS, 83, 119

Claussen M.J., Wilking B.A., Benson P.J., Wootten A., Myers P.C., Terebey, S., 1996, ApJS, 106, 111

Claussen M.J. et al., 1984, ApJL, 285, 79

Codella C., Palumbo G.G.C., Pareschi G., Scappini F., Caselli P., Attolini M.R., 1995, MNRAS, 276, 57

Codella C., Felli M., Natale V., Palagi F., Palla, F., 1994, A&A, 291, 261

Comoretto G. et al., 1990, A&AS, 84, 179

Dame T.M., Hartmann D., Thaddeus, P., 2001, ApJ, 547, 792

Deacon R.M., Chapman J.M., Green A.J., Sevenster, M.N., 2007, ApJ, 658, 1096

Deguchi S., Nakashima J., Kwok S., Koning, N., 2007, ApJ, 664, 1130

Deguchi S., Nakada Y., Forster, J.R., 1989, MNRAS, 239, 825

Di Francesco J., Johnstone D., Kirk H., MacKenzie T., Ledwosinska E., 2008, ApJS, 175, 277

Dickinson D.F., 1976, ApJS, 30, 259

Engels D., Schmid-Burgk J., Walmsley, C.M., 1986, A&A, 167, 129

Evans N.J.III, 1999, ARA&A, 37, 311

Felli M. et al., 2007, A&A, 476, 373

Forster J.R., Caswell J.L., 2000, ApJ, 530, 371

Forster J.R., Caswell J.L., 1999, A&AS, 137, 43

Forster J.R., Caswell J.L., 1989, A&A, 213, 339

Gaines L., Casleton K.H., Kukolich S.G., 1974, ApJL, 191, 99

Garay G., Moran J.M., Rodriguez L.F., Reid, M.J., 1998, ApJ, 492, 635

Genzel R., Downes D., 1979, A&A, 72, 234

Genzel R., Downes D., 1977 A&AS, 30, 145

Green J.A. et al., 2009, MNRAS, 392, 783

Healy K.R., Hester J.J., Claussen M.J., 2004, ApJ, 610, 835

Hinkle K.H., Barnes T.G., 1979, ApJ, 227, 923

Ho P.T.P., Townes C.H., 1983, ARA&A, 21, 239

Hunter T.R., Brogan C.L., Indebetouw R., Cyganowski, C.J., 2008, ApJ, 680, 1271

Imai H. et al., 2007, PASJ, 59, 1107

Jackson J.M. et al., 2006, ApJS, 163, 145

Jaffe D.T., Guesten R., Downes, D., 1981, ApJ, 250, 621

Jennings D.E., Fox K., 1982, ApJ, 254, 111

Johnston K.J., Sloanaker R.M., Bologna J.M., 1973, ApJ, 182, 67

Johnston K.J., Robinson B.J., Caswell J.L., Batchelor, R.A., 1972, ApL, 10, 93

Kaifu N., Suzuki H., Ohishi M., Miyaji T., Ishikawa S., Kasuga T., Morimoto M., Saito S., 1987, ApJL, 317, 111

Kaufmann P., Scalise E.Jr., Schaal R.E., Gammon R.H., Zisk, S., 1977, AJ, 82, 577

Kaufmann P. et al., 1976, Nature, 260, 306

Kazarovets E.V., Samus N.N., Durlevich O.V., Kireeva N.N., Pastukhova E.N. 2006, IBVS, 5721, 1

Kleinmann S.G., Sargent D.G., Dickinson, D.F., 1978, AJ, 83, 1206

Kolpak M.A., Jackson J.M., Bania T.M., Clemens D.P., Dickey, J.M., 2003 ApJ, 582, 756

Kraemer K.E., Jackson J.M., 1995, ApJL, 439, 9

Kukolich S.G., Wofsky, S.G., 1970, J. Chem. Phys., 52, 5477

Kukolich S.G., 1969, J. Chem. Phys., 50, 3751

Kukolich S.G., 1967, Phys. Rev., 156, 83

Lafferty W.J., Lovas F.J., 1978, J. Phys. Chem. Ref. Data, 7, 441

Le Bertre T., Tanaka M., Yamamura I., Murakami, H., 2003, A&A, 403, 943

Le Bertre T., Heydari-Malayeri M., Epchtein, N., 1988, A&A, 197, 143

Lilley A.E., Palmer P., 1967, ApJS, 16, 143

Longmore S.N., Burton M.G., Barnes P.J., Wong T., Purcell C.R., Ott, J., 2007, MNRAS, 379, 535

Mangum J.G., Wootten, A., 1994, ApJL, 428, 33

Matthews H.E., Olnon F.M., Winnberg A., Baud, B., 1985, A&A, 149, 227

McClure-Griffiths N.M., Dickey J.M., Gaensler B.M., Green A.J., Haverkorn M., Strasser, S., 2005, ApJS, 158, 178

Mehringer D.M., Goss W.M., Lis D.C., Palmer P., Menten K.M., 1998, ApJ, 493, 274

Mehrotra S.C., Dreizler H., Mäder, H., 1985, Z. Naturforschung, 40a, 683

Messineo M., Habing H.J., Sjouwerman L.O., Omont A., Menten K.M., 2002, A&A, 393, 115

Miranda L.F., Gómez Y., Anglada G., Torrelles, J.M., 2001, Nature, 414, 284

Müller H.S.P., Menten K.M., Mäder, H., 2004, A&A, 428, 1019

Nassau J.J., Blanco V.M., Morgan W.W., 1954, ApJ, 120, 478

Palagi F., Cesaroni R., Comoretto G., Felli M., Natale, V., 1993, A&AS, 101, 153

Palla F., Brand J., Comoretto G., Felli M., Cesaroni, R., 1991, A&A, 246 249

Peretto N., Fuller, G.A., 2009, A&A, 505, 405

Poynter R.L., Kakar R.K., 1975, ApJS, 29, 87

Reid, M.J. et al., 2009, ApJ, 700, 137

Santangelo G. et al., 2010, A&A, 520, 50

Scalise E.Jr., Rodriguez L.F., Mendoza-Torres, E., 1989, A&A, 221, 105

Schuller F. et al., 2009, A&A, 504, 415

Sevenster M.N., van Langevelde H.J., Moody R.A., Chapman J.M., Habing H.J., Killeen N.E.B., 2001, A&A, 366, 481

Sevenster M.N., Chapman J.M., Habing H.J., Killeen N.E.B., Lindqvist, M., 1997, A&AS, 124, 509

Sjouwerman L.O., Lindqvist M., van Langevelde H.J., Diamond P.J.,

Sloan G.C., Price S.D., 1998, ApJS, 119, 141

Stil J.M. et al., 2006, AJ, 132, 1158

Suárez O., Gómez J.F., Miranda L.F., Torrelles J.M., Gómez Y., Anglada G., Morata, O., 2009, A&A, 505, 217

Szymczak M., Pillai T., Menten, K.M., 2005, A&A, 434, 613

Szymczak M., Hrynek G., Kus A.J., 2000, A&AS, 143, 269

Tafalla M., Myers P.C., Caselli P., Walmsley C.M., Comito, C., 2002, ApJ, 569, 815

Taylor A.R. et al., 2003, AJ, 125, 3145

Taylor G.B., Morris M., Schulman E., 1993, AJ, 106, 1978

Thompson M.A., Hatchell J., Walsh A.J., MacDonald G.H., Millar T.J., 2006, A&A, 453, 1003

Urquhart J.S. et al., 2010, PASA, 27, 321

Urquhart J.S. et al., 2009, A&A, 507, 795

Voronkov M.A., Walsh A.J., Caswell J.L., Ellingsen S.P., Breen S.L., Longmore S.N., Purcell C.R., Urquhart J.S., 2011, MNRAS, *in press*

Voronkov M.A., Caswell J.L., Ellingsen S.P., Sobolev, A.M., 2010, MNRAS, 405, 2471

Walsh A.J., Breen S.L., Bains I., Vlemmings W.H.T., 2009, MNRAS Lett., 394, 70

Walsh A.J., Lo N. Burton M.G., White G.L., Purcell C.R., Longmore S.N., Phillips C.J., Brooks, K. J., 2008, PASA, 25, 105

Walsh A.J., Myers P.C., Di Francesco J., Mohanty S., Bourke T.L., Gutermuth R., Wilner D., 2007a, ApJ, 655, 958

Walsh A.J., Longmore S.N., Thorwirth S., Urquhart J.S., Purcell C.R., 2007b, MNRAS Lett., 382, 35

Walsh A.J., Macdonald G.H., Alvey N.D.S., Burton M.G., Lee, J.-K., 2003, A&A, 410, 597

Walsh A.J., Burton M.G., Hyland A.R., Robinson G., 1998, MNRAS, 301, 640

Walsh, A.J., Hyland A.R., Robinson G., Burton, M. G., 1997, MNRAS, 291, 261

Westerlund B.E., Olander, N., 1978, A&AS, 32, 401

Willacy K., Langer W.D., Velusamy, T., 1998, ApJL, 507, 171

Wood D.O.S., Churchwell E., 1989a, ApJS, 69, 831

Wood D.O.S., Churchwell E., 1989b, ApJ, 340, 265

Zhang Q., Ho P.T.P., 1995, ApJL, 450, 63